

Multi-Slice Low-Rank Tensor Decomposition Based Multi-Atlas Segmentation: Application to Automatic Pathological Liver CT Segmentation

Changfa Shi^{a,b}, Min Xian^{c,*}, Xiancheng Zhou^a, Haotian Wang^c,
Heng-Da Cheng^b

^aMobile E-business Collaborative Innovation Center of Hunan Province, Hunan University of Technology and Business, Changsha 410205, China

^bDepartment of Computer Science, Utah State University, Logan, UT 84322, USA

^cDepartment of Computer Science, University of Idaho, Idaho Falls, ID 83402, USA

Abstract

Liver segmentation from abdominal CT images is an essential step for liver cancer computer-aided diagnosis and surgical planning. However, both the accuracy and robustness of existing liver segmentation methods cannot meet the requirements of clinical applications. In particular, for the common clinical cases where the liver tissue contains major pathology, current segmentation methods show poor performance. In this paper, we propose a novel low-rank tensor decomposition (LRTD) based multi-atlas segmentation (MAS) framework that achieves accurate and robust pathological liver segmentation of CT images. Firstly, we propose a multi-slice LRTD scheme to recover the underlying low-rank structure embedded in 3D medical images. It performs the LRTD on small image segments consisting of multiple consecutive image slices. Then, we present an LRTD-based atlas construction method to generate tumor-free liver atlases that mitigates the performance degradation of liver segmentation due to the presence of tumors. Finally, we introduce an LRTD-based MAS algorithm to derive patient-specific liver atlases for each test image, and to achieve accurate pairwise image registration and label propagation. Extensive experiments on three public databases of pathological liver cases validate the effectiveness of the proposed method. Both qualitative and quantitative results demonstrate that, in the presence of major pathology, the proposed method is more accurate and robust than state-of-the-art methods.

Keywords: Pathological liver segmentation, Low-rank tensor decomposition, Multi-atlas segmentation, Tensor robust PCA, \star_M -product.

*Corresponding author. Tel: +1-208-757-5425.
Email address: mxian@uidaho.edu (Min Xian)

1. Introduction

According to GLOBOCAN 2018 estimates, liver cancer is the sixth most common cancer and the fourth leading cause of cancer mortality around the world (Bray et al., 2018). Liver segmentation (the extraction of the liver from its surrounding tissue) of abdominal computed tomography (CT) images is a key step and a prerequisite for liver cancer computer-aided diagnosis (CAD), surgical planning and other interventional procedures. However, in current clinical practice, liver segmentation from abdominal CT images is still predominantly performed manually by expert radiologists in a slice-by-slice manner. Due to the abundance of the CT images for each patient, the manual segmentation is time-consuming, and subject to observer error and personal bias. Therefore, it is highly desirable to develop fully automated liver segmentation approaches that can efficiently and automatically extract the liver boundary without any user intervention.

Numerous liver segmentation methods have been published in the last few decades. They can be generally classified into traditional image-based methods, model-based methods, and deep learning-based methods (Erdt et al., 2012). The traditional image-based methods are mainly relies on image intensity information to perform liver segmentation, such as intensity thresholding (Kobashi and Shapiro, 1995) and region growing (Ruskó et al., 2009), and they tend to have poor performance for clinical liver cases. The model-based methods, such as active shape model (ASM) (Heimann and Meinzer, 2009) and multi-atlas segmentation (MAS) (Iglesias and Sabuncu, 2015), have yielded remarkable results in liver CT segmentation (Heimann et al., 2009), where shape, appearance and spatial location information of the liver tissue were incorporated into the segmentation framework as prior knowledge. In recent years, deep learning-based methods achieve popularity in the field of medical image analysis due to their tremendous success in the computer vision community, and they have achieved state-of-the-art performance in medical image segmentation (Litjens et al., 2017). The main advantage of deep learning-based methods is that the most relevant features are automatically generated and selected for the given problem, rather than being manually engineered. However, when applied to liver CT image segmentation, the model-based methods proved to have comparable performance to deep learning-based methods (Ahn et al., 2019). The main reason is that the performance of deep learning-based methods highly depends on the availability of massive amounts of training data, which cannot be fully met in the case of liver CT image segmentation. Furthermore, compared to model-based methods, the interpretability of deep learning-based methods is poor, which, however, is of paramount importance in clinical applications.

Nevertheless, the drawback of aforementioned liver segmentation methods is that they still cannot meet the performance requirements of clinical applications. In particular, for common clinical cases where the liver tissue contains major pathology, current liver segmentation methods still show poor performance. It is mainly because the hypotheses of most current liver segmentation methods are only applicable to segment liver tissue of healthy or minor pathology conditions,

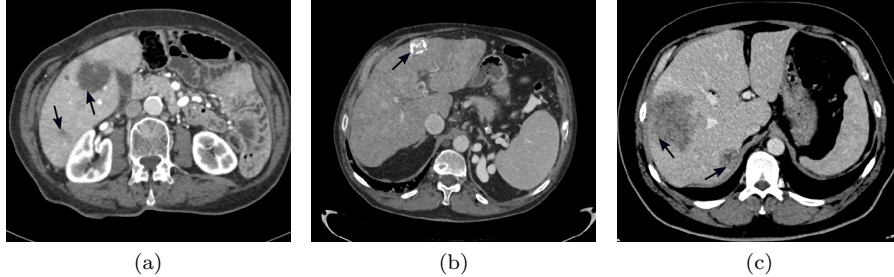


Figure 1: Examples demonstrating challenges in accurate and robust pathological liver segmentation in CT scans, consisting of liver tissue with (a) hypodense tumor, (b) hyperdense tumor, and (c) tumors located at liver boundary.

rather than of major pathology.

Specifically, the first challenge of pathological liver segmentation is the presence of large tumors, which exhibit totally different intensity values from that of the normal liver tissue. The large tumors can cause various undesired shape deformation of the liver tissue. Moreover, the tumors show very large variability of size and image appearance, resulting in tumors with different contrast levels, such as hypodense tumors (Fig. 1a) and hyperdense tumors (Fig. 1b). The second challenge of pathological liver segmentation is the complex spatial variability of tumors at liver boundary or inside liver parenchyma. In particular, when the tumors are at liver boundary (Fig. 1c), there is a very high probability that the peripheral liver tissue will be excluded from the final segmentation results, leading to under-segmentation. It is mainly due to the existence of blurred boundaries between the peripheral tumors and the nearby tissue (e.g., the muscle tissue) exhibiting similar image appearance.

Therefore, in the routine clinical setting, pathological liver segmentation is still mostly performed manually by expert radiologists, which is very labor-intensive, and subject to high intra- and inter-operator variability. Furthermore, since the liver tissue with large tumors exhibits totally different shape and image appearance from that of the normal liver tissue, it is also very challenging even for the expert radiologists to perform the segmentation task manually. Recently, a few pathological liver segmentation methods have been proposed in the literature (refer to Section 2.1 for a comprehensive survey). Nevertheless, the performance of these segmentation approaches is still unsatisfactory in the presence of major pathology.

In this paper, to address the above-mentioned issues, we integrate the general \star_M -product based low-rank tensor decomposition (LRTD) theory into the widely used MAS framework, and propose a novel automatic method for accurate and robust pathological liver segmentation of abdominal CT images. It is well-known that the segmentation accuracy of the MAS framework highly depends on the quality of the constructed atlases and pairwise image registra-

tions (Iglesias and Sabuncu, 2015). When employed to perform pathological liver CT segmentation, the main challenge to traditional MAS framework is the presence of large tumors, which exhibit totally different intensity values from that of the normal liver tissue, leading to liver atlases of low quality and large errors in pairwise image registrations. Inspired by the recently popular LRTD theory (Kolda and Bader, 2011), also known as Tensor Robust Principal Component Analysis (TRPCA) (Lu et al., 2020), in the fields of signal processing and computer vision, we first propose a multi-slice LRTD scheme for low-rank structure learning in 3D medical images. Specifically, we partition each liver CT image into smaller segments consisting of multiple consecutive image slices, and perform the LRTD on each segment sequentially. Then we present an LRTD-based atlas construction method to obtain tumor-free liver atlases that mitigate the performance degradation of liver segmentation caused by the presence of tumors. Specifically, given a data tensor \mathcal{D} , the LRTD model decomposes it into two parts: (1) a low-rank component \mathcal{L} corresponding to the tumor-free liver images via tensor rank minimization, and (2) a sparse component \mathcal{E} corresponding to the sparse tumors via ℓ_0 -norm minimization. Thus, the LRTD model fits the goal of deriving tumor-free liver images very well. Furthermore, we introduce an LRTD-based MAS algorithm to derive patient-specific liver atlases for each test image, and to yield accurate pairwise image registration and label propagation.

In order to evaluate the performance of our proposed MAS-based segmentation framework, and to show its clinical applicability to pathological liver segmentation, we extensively tested it using three public clinical CT databases, and also compared it with state-of-the-art methods. The experimental results demonstrate that the proposed method yields higher accuracy and robustness than that of state-of-the-art methods.

The main contributions of the proposed LRTD-based MAS framework can be summarized as follows:

- (1) A general multi-slice LRTD scheme is proposed to recover the underlying low-rank structure embedded in 3D medical images. In particular, the discrete cosine transform (DCT) converts the calculation of tensor singular value decomposition (t-SVD) to matrix SVD in the transform domain, which enhances the computational efficiency and maintains spatial relationship. Then the tensor singular value thresholding (t-SVT) algorithm is used to recover the underlying low-rank structure. The general scheme is also applicable to other medical imaging modalities and organs (Qin et al. (2019); Xian et al. (2018); Khaleel et al. (2018)) (Section 4.1).
- (2) An LRTD-based atlas construction method is developed to produce tumor-free liver atlases. In the MAS framework, atlases with tumor regions will lead to inaccurate pairwise image registration and performance degradation (Section 4.1).
- (3) An LRTD-based MAS algorithm is proposed to achieve more accurate and robust liver segmentation. An atlas selection strategy is first implemented

to obtain patient-specific liver atlases for each test image. Then, based on the selected tumor-free liver atlases, it generates a tumor-free test image that yields accurate pairwise image registration and label propagation (Section 4.2).

- (4) We conducted extensive experiments to compare the proposed method to state-of-the-art methods using three public clinical CT databases. It is shown that our method is more accurate and robust than state-of-the-art methods in the presence of major pathology (Section 6).

2. Related Work

2.1. Pathological Liver CT Segmentation

Li et al. (2020) proposed a pathological liver CT segmentation method by combining level set, sparse shape composition, and graph cut methods. The initial liver shape was obtained by a level set method integrated with intensity bias and position constraint, followed by sparse shape composition and graph cut based segmentation refinements. Raju et al. (2020) proposed a user-guided domain adaptation framework for pathological liver CT segmentation, which used prediction-based adversarial domain adaptation to guide mask predictions by the user interactions. Dakua et al. (2016) proposed a semi-automatic method for pathological liver CT segmentation, where a stochastic resonance algorithm was utilized to enhance the contrast of the liver images, followed by cellular automaton and level set segmentation methods. Umetsu et al. (2014) proposed a graph cut based method for segmenting liver CT cases with unusual shapes and pathological lesions, where a sparse representation based patient-specific probabilistic atlas reinforced by the lesion bases was incorporated with the graph cut method. Nevertheless, in the presence of major pathology, the performance of the above-mentioned liver CT segmentation methods is still not satisfactory, and further improvements are needed.

2.2. Low-Rank Tensor Decomposition for Medical Image Computing

The LRTD theory has been widely studied and applied in the fields of signal processing and computer vision (Sidiropoulos et al., 2017; Cichocki et al., 2015; Sobral and Zahzah, 2017). Recently, it has gained wide applications in the field of medical image computing (Madathil et al., 2019), including medical image reconstruction, super-resolution, denoising, and analysis. The images from most medical imaging modalities are currently acquired as 3D volumes, such as CT, Magnetic Resonance (MR). Since the LRTD models the 3D volumes in their native format (i.e., tensor) rather than vectorizing them into 1D vectors, it can simultaneously exploits both the spatial and temporal correlations embedded in the 3D volumes (Madathil et al., 2019).

Liu et al. (2020) and Roohi et al. (2017) proposed multi-dimensional approaches to the problem of dynamic MRI reconstruction of under-sampled k-space by formulating it as an LRTD problem, and the recovery performance

was superior to that of other reconstruction methods. Shi et al. (2015) proposed an MR image super-resolution method that integrated both local and global information for effective image recovery via total variation and low-rank tensor regularizations, respectively. A few LRTD-based image denoising methods were proposed for MR (Khaleel et al., 2018; Fu and Dong, 2016) and CT images (Sagheer and George, 2019) to reduce noise and artifacts introduced during image acquisition. Jiang et al. (2020) proposed a functional connectivity network estimation approach by the assumption that the functional connectivity networks have similar topology across subjects via the LRTD. Qin et al. (2019) proposed an LRTD-based method for accurately recovering vessel structures and intensity information from the X-ray coronary angiography (XCA) sequences. Xu et al. (2016) proposed an LRTD-based one-step method for axial alignment in 360-degree anterior chamber optical coherence tomography. To the best of our knowledge, the proposed method is the first MAS framework directly utilizing the LRTD for medical image segmentation.

2.3. Relation to Previous Work

The proposed LRTD-based MAS framework is partly inspired by two recent papers (Liu et al. (2015) and Shi et al. (2017)). They both proposed an atlas-based organ segmentation method by utilizing low-rank matrix decomposition (LRMD) theory (Zhou et al., 2014) to handle clinical cases with pathology. In this study, we significantly extend their methods in the following directions:

- (1) We propose a new MAS framework based on the LRTD, rather than the LRMD as in their original methods. To perform the LRMD, the 3D data tensor is first reformatted to a matrix by vectorizing voxel intensity values of each CT scan to form the column vectors. The local spatial information is thus completely lost, and the multi-dimensional structure embedded in the tensor data is disregarded, leading to considerable performance degradation. While our tensor-based method can fully exploit the intrinsic three-dimensional structural information of the CT scans, resulting in much more accurate data decomposition results.
- (2) The whole image volumes were directly employed to perform the LRMD in their original methods, whereas we propose a new multi-slice LRTD scheme, where each liver CT image is first partitioned into smaller segments consisting of multiple consecutive image slices, then the LRTD is performed on each segment sequentially. Since smaller image segment exhibits fewer overall structural changes, it will lie on a low-rank subspace (Lee et al., 2018). It can thus yield more accurate data decomposition results than directly performing the LRMD on whole image volumes.

3. Mathematical Notations and Tensor Preliminaries

In this section, the notations and preliminaries of tensor used in the rest of the paper are briefly described. Throughout this paper, we follow the notation

and terminology of Kolda and Bader (2011), Lu et al. (2019) and Kilmer et al. (2019).

3.1. Mathematical Notations

A third-order tensor and its entries are denoted by capital boldface Euler script letters and small symbols, respectively, e.g., x_{ijk} is the (i, j, k) -th entry of the tensor $\mathcal{X} \in \mathbb{R}^{n_1 \times n_2 \times n_3}$. Matrix is denoted by capital boldface letters, e.g., $\mathbf{X} \in \mathbb{R}^{n_1 \times n_2}$. The two-dimensional horizontal, lateral, and frontal slices of a third-order tensor \mathcal{X} are denoted by $\mathcal{X}(i, :, :)$, $\mathcal{X}(:, j, :)$, and $\mathcal{X}(:, :, k)$, respectively. The frontal slices are often denoted more compactly as $\mathbf{X}^{(k)}$, i.e., $\mathbf{X}^{(k)} = \mathcal{X}(:, :, k)$. The mode- k fibers of a third-order tensor \mathcal{X} are vectors defined by fixing all indices but the k -th, e.g., the mode-3 fibers are denoted by $\mathcal{X}(i, j, :)$.

The inner product between two matrices is defined as $\langle \mathbf{X}, \mathbf{Y} \rangle = \text{tr}(\mathbf{X}^* \mathbf{Y})$, where \mathbf{X}^* and $\text{tr}(\cdot)$ denote the conjugate transpose of \mathbf{X} and the matrix trace, respectively. The inner product between two tensors can then be defined as $\langle \mathcal{X}, \mathcal{Y} \rangle = \sum_{k=1}^{n_3} \langle \mathbf{X}^{(k)}, \mathbf{Y}^{(k)} \rangle$. Three tensor norms are used: $\|\mathcal{X}\|_0$ the ℓ_0 -norm (i.e., the number of non-zero entries in \mathcal{X}), $\|\mathcal{X}\|_1 = \sum_{ijk} |x_{ijk}|$ the ℓ_1 -norm, and $\|\mathcal{X}\|_\infty = \max_{ijk} |x_{ijk}|$ the infinity norm.

3.2. Tensor Preliminaries

Mode-3 product. The mode-3 product (\times_3) is an operator between a tensor $\mathcal{X} \in \mathbb{R}^{n_1 \times n_2 \times n_3}$ and a matrix $\mathbf{M} \in \mathbb{R}^{n_3 \times n_3}$. The result is another tensor $\bar{\mathcal{X}} \in \mathbb{R}^{n_1 \times n_2 \times n_3}$ defined as the following (Kolda and Bader, 2011):

$$\bar{\mathcal{X}} = \mathcal{X} \times_3 \mathbf{M} = \mathbf{M} \cdot \mathcal{X}_{(3)}, \quad (1)$$

where $\mathcal{X}_{(3)} \in \mathbb{R}^{n_3 \times n_1 n_2}$ denotes the mode-3 unfolding of \mathcal{X} , defined as a matrix whose columns consist of the mode-3 fibers. The mode-3 product can be interpreted geometrically as performing a linear transform on \mathcal{X} along the third dimension via transform matrix \mathbf{M} . We can denote it more compactly as $\mathbf{M}(\mathcal{X})$.

t-product. The t-product ($*$) between two tensors $\mathcal{X} \in \mathbb{R}^{n_1 \times n_2 \times n_3}$ and $\mathcal{Y} \in \mathbb{R}^{n_2 \times m \times n_3}$ is a multiplication operator that preserves the order of the tensor. The result tensor $\mathcal{Z} \in \mathbb{R}^{n_1 \times m \times n_3}$ is defined as following (Kilmer and Martin, 2011):

$$\mathcal{Z} = \mathcal{X} * \mathcal{Y} = \text{fold}(\text{bcirc}(\mathcal{X}) \cdot \text{unfold}(\mathcal{Y})), \quad (2)$$

where $\text{bcirc}(\mathcal{X}) \in \mathbb{R}^{n_1 n_3 \times n_2 n_3}$ is a block circulant matrix, which can be regarded as a new matricization of \mathcal{X} , fold and unfold are a pair of operators on tensors (see Eq. A.1 and Eq. A.2 in Appendix A).

For tensor $\mathcal{X} \in \mathbb{R}^{n_1 \times n_2 \times n_3}$, its discrete Fourier transform (DFT) along the third dimension is denoted as $\bar{\mathcal{X}} = \mathcal{X} \times_3 \mathbf{F}_{n_3} = \mathbf{F}_{n_3}(\mathcal{X})$, where $\mathbf{F}_{n_3} \in \mathbb{C}^{n_3 \times n_3}$ is the DFT matrix. By using Matlab convention, we also have $\bar{\mathcal{X}} = \text{fft}(\mathcal{X}, [], 3)$. Conversely, \mathcal{X} can be derived from $\bar{\mathcal{X}}$ via inverse DFT, i.e., $\mathcal{X} = \bar{\mathcal{X}} \times_3 \mathbf{F}_{n_3}^{-1} =$

$\mathbf{F}_{n_3}^{-1}(\mathcal{X}) = \text{ifft}(\bar{\mathcal{X}}, [], 3)$. The block circulant matrix $\text{bcirc}(\mathcal{X})$ can be block-diagonalized to a special block diagonal matrix $\bar{\mathbf{X}}$, whose main diagonal blocks are the frontal slices of $\bar{\mathcal{X}}$ (see Eq. A.3 in Appendix A), via the DFT matrix $\mathbf{F}_{n_3} \in \mathbb{C}^{n_3 \times n_3}$ (Kolda and Bader, 2011):

$$(\mathbf{F}_{n_3} \otimes \mathbf{I}_{n_1}) \cdot \text{bcirc}(\mathcal{X}) \cdot (\mathbf{F}_{n_3}^{-1} \otimes \mathbf{I}_{n_2}) = \bar{\mathbf{X}}, \quad (3)$$

where \otimes denotes the Kronecker product.

Based on the block-diagonalized property of $\text{bcirc}(\mathcal{X})$ in Eq. 3, the t-product can also be defined as the matrix-matrix product in the DFT domain (Lu et al., 2020):

$$\mathcal{Z} = (\bar{\mathcal{X}} \Delta \bar{\mathcal{Y}}) \times_3 \mathbf{F}_{n_3}^{-1} = \mathbf{F}_{n_3}^{-1} (\mathbf{F}_{n_3}(\mathcal{X}) \Delta \mathbf{F}_{n_3}(\mathcal{Y})), \quad (4)$$

where Δ denotes the face-wise product, defined as the matrix-matrix product between corresponding frontal slices of the two tensors.

\star_M -product. A new tensor-tensor product operator, called \star_M -product, is proposed in Kilmer et al. (2019). It can convert the data into other transform domains under any invertible matrix \mathbf{M} , rather than the specific DFT domain as in the t-product. The superiority of \star_M -product compared to the t-product is demonstrated in Kilmer et al. (2019).

Let $\mathbf{M} \in \mathbb{R}^{n_3 \times n_3}$ be any invertible matrix satisfying:

$$\mathbf{M}^* \mathbf{M} = \mathbf{M} \mathbf{M}^* = l \mathbf{I}_{n_3}, \quad (5)$$

where $l > 0$ is a constant, $\mathcal{X} \in \mathbb{R}^{n_1 \times n_2 \times n_3}$ and $\mathcal{Y} \in \mathbb{R}^{n_2 \times m \times n_3}$ are two tensors. Then the \star_M -product $\mathcal{X} \star_M \mathcal{Y}$ results in a tensor $\mathcal{Z} \in \mathbb{R}^{n_1 \times m \times n_3}$ defined as below (Kilmer et al., 2019; Lu et al., 2019):

$$\mathcal{Z} = \mathcal{X} \star_M \mathcal{Y} = (\bar{\mathcal{X}} \Delta \bar{\mathcal{Y}}) \times_3 \mathbf{M}^{-1} = \mathbf{M}^{-1} (\mathbf{M}(\mathcal{X}) \Delta \mathbf{M}(\mathcal{Y})), \quad (6)$$

where $\bar{\mathcal{X}} = \mathbf{M}(\mathcal{X}) = \mathcal{X} \times_3 \mathbf{M}$ denotes the tensor in the transform domain induced by the invertible transformation matrix \mathbf{M} . Note that the t-product becomes a special case of the \star_M -product when $\mathbf{M} = \mathbf{F}_{n_3}$.

Based on the \star_M -product, the following main concepts of tensor can be defined: conjugate transpose, identity tensor, orthogonal tensor, and f-diagonal tensor (see Appendix A). Also, we can obtain the following theorem defining the tensor SVD (t-SVD):

Theorem 1 (T-SVD Kilmer et al. (2019)). *Let $\mathcal{X} \in \mathbb{R}^{n_1 \times n_2 \times n_3}$, and $\mathbf{M} \in \mathbb{R}^{n_3 \times n_3}$ be any invertible matrix. Then \mathcal{X} can be factorized as:*

$$\mathcal{X} = \mathcal{U} \star_M \mathcal{S} \star_M \mathcal{V}^*, \quad (7)$$

where $\mathcal{U} \in \mathbb{R}^{n_1 \times n_1 \times n_3}$ and $\mathcal{V} \in \mathbb{R}^{n_2 \times n_2 \times n_3}$ are orthogonal tensors, and $\mathcal{S} \in \mathbb{R}^{n_1 \times n_2 \times n_3}$ is an f-diagonal tensor.

An illustration of the t-SVD factorization is shown in Fig. A.9 in Appendix A. Empirically, we can obtain the factorization results by computing matrix SVDs in the transform domain, refer Algorithm 3 in Appendix A.

Tensor nuclear norm. The minimization of the tensor rank is known as NP-hard due to the non-convexity nature (Hillar and Lim, 2013). Fortunately, as in the matrix case, the tensor nuclear norm can be employed as a convex relaxation of the tensor rank for the LRTD (Lu et al., 2019).

Let $\mathbf{M} \in \mathbb{R}^{n_3 \times n_3}$ be any invertible matrix satisfying Eq. 5, the tensor nuclear norm of $\mathcal{X} \in \mathbb{R}^{n_1 \times n_2 \times n_3}$ is defined as $\|\mathcal{X}\|_* = \frac{1}{I} \sum_{i=1}^{n_3} \|\bar{\mathbf{X}}^{(i)}\|_*$ (Lu et al., 2019). It has been proven that the tensor nuclear norm $\|\mathcal{X}\|_*$ is the convex envelop of the tensor average rank $\text{rank}_a(\mathcal{X}) = \frac{1}{I} \sum_{i=1}^{n_3} \text{rank}(\bar{\mathbf{X}}^{(i)})$ within the unit ball of the tensor spectral norm $\|\mathcal{X}\| = \|\bar{\mathbf{X}}\|$ (Lu et al., 2019). We will thus use the tensor nuclear norm $\|\cdot\|_*$ to characterize the low-rank latent structure of a tensor.

4. Methods

The main workflow of the proposed segmentation framework is depicted in Fig. 2. In the training stage, two models used in the MAS framework are constructed: population-specific probabilistic atlas (PA) and tumor-free liver atlases (Section 4.1). In the testing stage, for a given test abdominal CT image, we first implement an atlas selection strategy to derive patient-specific liver atlases, then generate a tumor-free test image based on the selected tumor-free liver atlases, and finally perform the main steps of the MAS algorithm to extract the liver tissue from the tumor-free test image (Section 4.2).

4.1. Low-Rank Tensor Decomposition for Liver Atlas Construction

To derive patient-specific liver atlases, and to substantially reduce the computational cost of the MAS framework, we propose an LRTD-based liver atlas construction method. Specifically, we first group the training data into multiple smaller clusters corresponding to different type cases, then construct a population-specific PA and tumor-free liver atlases for each cluster separately.

4.1.1. Population-Specific PA and Tumor-Free Liver Atlases

We first employ the same spectral clustering based algorithm (von Luxburg, 2007) as in Shi et al. (2017). It involves two major steps: (1) training data alignment: Since the similarity measure used in the clustering step is based on both intensity images and liver shapes, the training data needs to be first aligned; and (2) data clustering using the spectral clustering algorithm. Please refer to Shi et al. (2017) for details.

After the training data is partitioned into multiple clusters, we construct a population-specific PA and tumor-free liver atlases for each cluster separately. Nevertheless, most of the training images include major pathology. To mitigate the performance degradation of liver segmentation due to the presence of tumors in the constructed atlases, we cast the procedure of generating tumor-free liver atlases as an LRTD problem (Kolda and Bader, 2011), also known as TRPCA (Lu et al., 2020). Specifically, we propose an LRTD-based liver atlas construction method, called LRTD-PA, based on the following two empirical

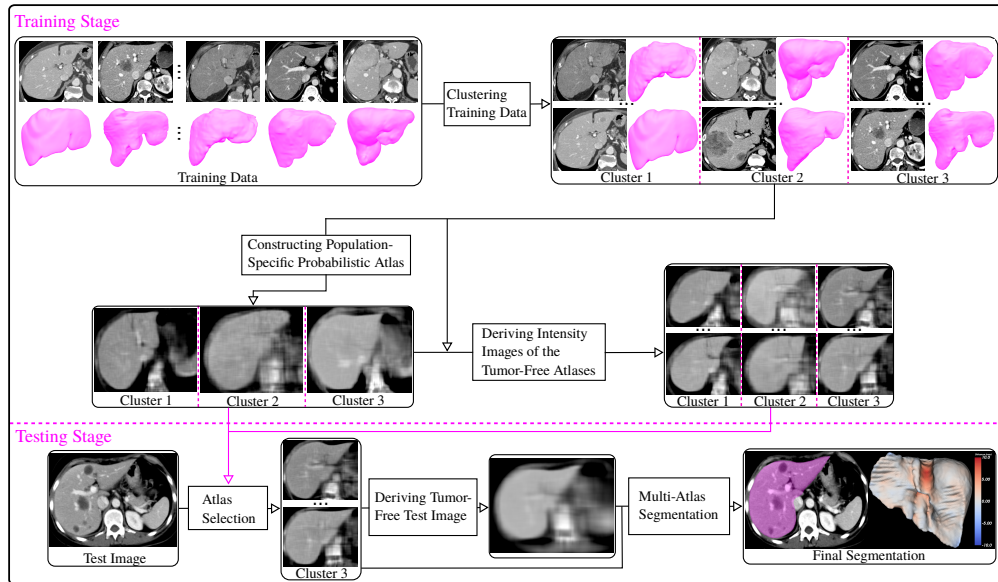


Figure 2: The main workflow of the proposed framework for pathological liver CT segmentation, consisting of training and testing stages.

observations: (1) the aligned training images are linearly correlated with each other and form a low-rank third-order tensor (Sagheer and George, 2019); and (2) the portions that cannot be represented by the low-rank part are the gross errors or outliers (e.g., tumors), which can also be considered sparse compared to the whole image tensor.

Let $\{I_i \mid i = 1, \dots, N_c\}$ be the pre-aligned training images with their corresponding label images $\{L_i \mid i = 1, \dots, N_c\}$ of cluster c . We represent each training image I_i as a third-order image tensor $\mathcal{D}_i \in \mathbb{R}^{w \times h \times d}$ by stacking all voxel intensity values of the axial slices frontal-slice-wisely, where w , h and d denote the width, height and the number of axial CT slices, respectively. Then we construct a third-order image repository tensor $\mathcal{X} \in \mathbb{R}^{w \times h \times (dN_c)}$ by concatenating all training image tensors $\{\mathcal{D}_i \mid i = 1, \dots, N_c\}$ frontal-slice-wisely. Mathematically, the LRTD model decomposes the image repository tensor \mathcal{X} into two components according to the following minimization:

$$(\hat{\mathcal{L}}, \hat{\mathcal{E}}) = \arg \min_{\mathcal{L}, \mathcal{E}} \text{rank}(\mathcal{L}) + \lambda \|\mathcal{E}\|_0 \quad \text{s. t.} \quad \mathcal{X} = \mathcal{L} + \mathcal{E}, \quad (8)$$

where \mathcal{L} represents the low-rank component corresponding to the tumor-free training images via tensor rank minimization, \mathcal{E} represents the sparse component corresponding to the sparse tumors via ℓ_0 -norm minimization, and λ is a trade-off factor between the two components. Since \mathcal{E} is employed to explicitly model the sparse gross errors via the ℓ_0 -norm, the LRTD model fits the purpose

of generating tumor-free training images very well, and our proposed LRTD-PA is robust to handle major pathology.

Nevertheless, the minimization problem in Eq. 8 is known to be computationally intractable (NP-hard), due to the non-convex property of the tensor rank and ℓ_0 -norm (Hillar and Lim, 2013; Natarajan, 1995). Fortunately, it has been proven that solving the following relaxed dual convex minimization problem, called Tensor Principal Component Pursuit (TPCP) (Zhang et al., 2020b; Lu et al., 2020), can achieve the same decomposition accuracy:

$$(\hat{\mathcal{L}}, \hat{\mathcal{E}}) = \arg \min_{\mathcal{L}, \mathcal{E}} \|\mathcal{L}\|_* + \lambda \|\mathcal{E}\|_1 \quad \text{s. t.} \quad \mathcal{X} = \mathcal{L} + \mathcal{E}, \quad (9)$$

where the tensor nuclear norm $\|\cdot\|_*$ is defined as in Section 3.2. The tensor nuclear norm and ℓ_1 -norm are the convex surrogates of the tensor rank and ℓ_0 -norm, respectively. Under certain incoherence conditions, it has been proven that TPCP can exactly recover the underlying low-rank \mathcal{L} and sparse \mathcal{E} components with high probability (Lu and Zhou, 2019).

However, empirically we find that when performing the LRTD directly on the image repository tensor \mathcal{X} that consists of all slices of the training images, the results are unsatisfactory. It is mainly because the differences between consecutive image slices in terms of both background and liver tissue accumulate along the axial direction, resulting in overall rapid changes over the whole image volume. The image repository tensor \mathcal{X} thus does not possess strong low-rank property any more. We hypothesize that performing the LRTD on smaller segments consisting of multiple consecutive image slices can lead to better results, since smaller segments exhibit fewer overall changes, they will lie on a low-rank subspace (Lee et al., 2018). Furthermore, both the computational cost and memory usage will be reduced substantially. To this end, we propose a multi-slice LRTD scheme to recover the underlying low-rank structure embedded in 3D medical images. Specially, we first partition each training image tensor \mathcal{D}_i into smaller segments $\{\mathcal{D}_{ij} \mid j = 1, \dots, N_s\}$ consisting of multiple consecutive image slices of length K , then construct a third-order image repository tensor \mathcal{X}_j for each segment $\{\mathcal{D}_{ij} \mid i = 1, \dots, N_c\}$ frontal-slice-wisely, and finally perform the LRTD on each segment tensor \mathcal{X}_j sequentially. Mathematically, the multi-slice LRTD scheme solves the following minimization for each segment tensor \mathcal{X}_j :

$$(\hat{\mathcal{L}}_j, \hat{\mathcal{E}}_j) = \arg \min_{\mathcal{L}_j, \mathcal{E}_j} \|\mathcal{L}_j\|_* + \lambda \|\mathcal{E}_j\|_1 \quad \text{s. t.} \quad \mathcal{X}_j = \mathcal{L}_j + \mathcal{E}_j. \quad (10)$$

Eq. 10 is the optimization problem of proposed liver atlas construction method LRTD-PA, through which the tumor-free training images lie in the low-rank component $\hat{\mathcal{L}}_j$, while the tumors are extracted in $\hat{\mathcal{E}}_j$. After obtaining $\{(\hat{\mathcal{L}}_j, \hat{\mathcal{E}}_j) \mid j = 1, \dots, N_s\}$, we separately stack them frontal-slice-wisely to obtain $\hat{\mathcal{L}}$ and $\hat{\mathcal{E}}$. The tumor-free training images in the low-rank component $\hat{\mathcal{L}}$ are employed to construct the population-specific PA \bar{I}_c , from which we can then obtain intensity images of the tumor-free liver atlases $\{\hat{I}_i \mid i = 1, \dots, N_c\}$. Fig.

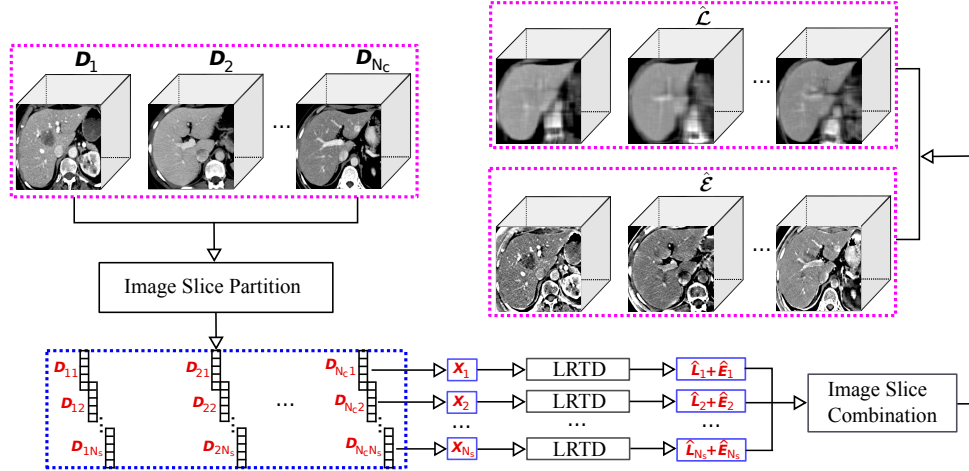


Figure 3: An example of the multi-slice LRTD applied to training images of cluster c . All training image tensors $\{\mathcal{D}_i \mid i = 1, \dots, N_c\}$ are first partitioned into smaller segments $\{\mathcal{D}_{ij} \mid j = 1, \dots, N_s\}$ consisting of multiple consecutive image slices of length $K = 5$, then the LRTD is performed on each segment tensor \mathcal{X}_j sequentially, and finally the decomposed low-rank and sparse components of all the segment tensors are separately combined to obtain tumor-free training images $\hat{\mathcal{L}}$ and tumor images $\hat{\mathcal{E}}$.

3 shows an example of the multi-slice LRTD applied to the training images of cluster c . The iterative procedure for constructing population-specific PA and tumor-free liver atlases for each cluster using proposed LRTD-PA is summarized in Algorithm 1. Note that since the LRTD is performed in a segment-by-segment fashion, to maintain a smooth transition between neighboring segments in the tumor-free training images, we expand each segment to overlap with one neighboring slice at each end, and average the decomposition results in overlapping slices. Thus the smallest possible segment length K is 2.

4.1.2. Optimization

In the past few years, many optimization algorithms have been proposed to solve the LRTD problem (Sidiropoulos et al., 2017), and stable recovery of the low-rank \mathcal{L} and sparse \mathcal{E} components can be guaranteed (Lu and Zhou, 2019; Zhang et al., 2020a). To achieve both efficiency and scalability, we use the alternating direction method of multipliers (ADMM) algorithm (Boyd et al., 2010; Lu et al., 2020) to solve the TPCP problem in Eq. 10. The ADMM algorithm is a first-order optimization method where both the objective function and the constraints exhibit separable structures. It has been widely utilized for solving convex optimization problems with well-established convergence properties (Boyd et al., 2010).

Algorithm 4 (Appendix B) summarizes the derived ADMM algorithm for

Algorithm 1 Population-Specific Probabilistic Atlas and Tumor-Free Liver Atlases Construction Procedure

Input: Training images of class c : $\{I_i \mid i = 1, \dots, N_c\}$, and the maximum number of iterations: N_{max} .

Output: The probability atlas \bar{I}_c , and intensity images of the tumor-free liver atlases $\{\hat{I}_i \mid i = 1, \dots, N_c\}$ for class c .

1. Select the training image containing smallest tumor region as the initial template \bar{I}^0 .

2. Compute the non-rigid transformation T_i^0 that warps I_i to the template \bar{I}^0 : $I_i^1 \leftarrow T_i^0(I_i), i = 1, \dots, N_c$, and obtain the corresponding third-order image tensors: $\mathcal{D}_i^1 \leftarrow I_i^1, i = 1, \dots, N_c$.

3. Obtain the population-specific probability atlas iteratively:

for $k = 1$ **to** N_{max} **do**

3.1 Compute low-rank parts via multi-slice LRTD on \mathcal{X} :

$$[I_{LR1}^k, I_{LR2}^k, \dots, I_{LRN_c}^k] \leftarrow \text{MS-LRTD}(\mathcal{X} = [\mathcal{D}_1^k, \mathcal{D}_2^k, \dots, \mathcal{D}_{N_c}^k]).$$

3.2 Obtain the new template using low-rank parts: $\bar{I}^k \leftarrow \frac{1}{N_c} \sum_{n=1}^{N_c} I_{LRn}^k$.

3.3 Compute the non-rigid transformation T_i^k that warps I_{LRi}^k to the template $\bar{I}^k, i = 1, \dots, N_c$.

3.4 Align I_i^k to the space of the template \bar{I}^k using T_i^k : $I_i^{(k+1)} \leftarrow T_i^k(I_i^k), i = 1, \dots, N_c$, and obtain the corresponding third-order image tensors: $\mathcal{D}_i^{(k+1)} \leftarrow I_i^{(k+1)}, i = 1, \dots, N_c$.

end for

$$\bar{I}_c \leftarrow \bar{I}^{N_{max}}.$$

4. Generate the tumor-free liver atlases of class c :

4.1 Compute the non-rigid transformation T_i that warps I_i to the probability atlas \bar{I}_c : $I_i' \leftarrow T_i(I_i), i = 1, \dots, N_c$, and obtain the corresponding third-order image tensors: $\mathcal{D}_i' \leftarrow I_i', i = 1, \dots, N_c$.

4.2 Compute low-rank parts via multi-slice LRTD on \mathcal{X}' :

$$[I'_{LR1}, I'_{LR2}, \dots, I'_{LRN_c}] \leftarrow \text{MS-LRTD}(\mathcal{X}' = [\mathcal{D}'_1, \mathcal{D}'_2, \dots, \mathcal{D}'_{N_c}]).$$

4.3 $\hat{I}_i \leftarrow T_i^{-1}(I'_{LRi}), i = 1, \dots, N_c$.

solving the TPCP problem (Eq. 10) in the proposed liver atlas construction method LRTD-PA. The detailed mathematical derivation procedure is given in Appendix B. Algorithm 5 (Appendix B) shows the optimization procedure of the proposed multi-slice LRTD scheme. The convergence properties of the ADMM algorithm with two blocks, as in this study, have been well established (Boyd et al., 2010). Suppose that the size of the data tensor \mathcal{X} is $n_1 \times n_2 \times n_3$ with $n_1 \geq n_2$, the main computational cost of the ADMM algo-

rithm lies in computing the t-SVT operator \mathbf{D}_τ in the \mathcal{L} subproblem (Eq. B.5 in Appendix B). For any general invertible matrix $\mathbf{M} \in \mathbb{R}^{n_3 \times n_3}$, the per-iteration computational complexity of the ADMM algorithm is $O(n_1 n_2 n_3^2 + n_1 n_2^2 n_3)$ (Lu and Zhou, 2019).

4.2. LRTD-Based MAS Algorithm

After the tumor-free liver atlases are constructed, we propose an LRTD-based MAS algorithm to perform liver CT segmentation. Specifically, given a test image I_t , we first implement an atlas selection strategy to obtain patient-specific liver atlases, and to substantially improve the computational efficiency. Then based on intensity images of the selected tumor-free liver atlases, we generate a tumor-free test image I_{LR_t} . Finally, the main steps of the MAS algorithm are performed to extract the liver tissue from I_{LR_t} .

Considering that the liver tissue exhibits high anatomical variability, we construct patient-specific liver atlases for each test image via an atlas selection strategy (Shi et al., 2017) to achieve more accurate liver segmentation. Specifically, we first choose the best training data cluster based on the similarity between the test image I_t and the population-specific PAs. The cluster c is selected when the normalized cross correlation (NCC) between I_t and the population-specific PA \bar{I}_c after its warping into the space of I_t , i.e., $NCC(\bar{I}_c, I_t)$, is the largest. The NCC between two images I_i and I_j is defined as:

$$NCC(I_i, I_j) = \frac{\sum_{\mathbf{x} \in \Omega} (I_i(\mathbf{x}) - \bar{I}_i) (I_j(\mathbf{x}) - \bar{I}_j)}{\sqrt{\sum_{\mathbf{x} \in \Omega} (I_i(\mathbf{x}) - \bar{I}_i)^2} \sqrt{\sum_{\mathbf{x} \in \Omega} (I_j(\mathbf{x}) - \bar{I}_j)^2}}, \quad (11)$$

where \bar{I}_i and \bar{I}_j denote the mean values of the images within the overlapping region Ω . Then the tumor-free intensity images and their corresponding label images within the chosen cluster c are regarded as the patient-specific liver atlases for the test image I_t .

Generally, the test image I_t is directly employed to perform image registrations in the MAS algorithm. However, we empirically find that most of the test images contain tumors. In order to achieve accurate pairwise image registration and label propagation, we use the proposed LRTD-PA to generate a tumor-free test image I_{LR_t} . Specifically, given the test image I_t , we first construct a third-order data tensor $\mathcal{X}_t \in \mathbb{R}^{w \times h \times (d(N_c+1))}$ by concatenating the warped image repository tensor of the chosen cluster $\mathcal{X}' \in \mathbb{R}^{w \times h \times (dN_c)}$ with the test image tensor $\mathcal{D}_t \in \mathbb{R}^{w \times h \times d}$ frontal-slice-wisely. After performing the multi-slice LRTD on the data tensor \mathcal{X}_t , we can obtain the tumor-free test image I_{LR_t} , as shown in Algorithm 2. Fig. 4 shows an example of generating the tumor-free image I_{LR_t} for a test image I_t using the proposed LRTD-PA.

After obtaining the tumor-free test image I_{LR_t} , it is the input to the MAS algorithm. The main steps of the MAS algorithm (i.e., image registration, label propagation, and label fusion) are then performed to obtain the liver segmentation result.

Algorithm 2 Tumor-Free Test Image Derivation Procedure

Input: Intensity images of the tumor-free atlases within the chosen cluster c : $\{\hat{I}_i \mid i = 1, \dots, N_c\}$, the test image: I_t , and the maximum number of iterations: N_{max} .

Output: The tumor-free test image I_{LR_t} .

1. Compute the non-rigid transformation T_i^0 that warps \hat{I}_i to the target image I_t : $\hat{I}_i^1 \leftarrow T_i^0(\hat{I}_i), i = 1, \dots, N_c$, and obtain the corresponding third-order image tensors: $\hat{\mathcal{D}}_i^1 \leftarrow \hat{I}_i^1, i = 1, \dots, N_c$.

2. Obtain the test image tensor: $\mathcal{D}_t \leftarrow I_t$.

3. Obtain the tumor-free test image iteratively:

for $k = 1$ **to** N_{max} **do**

3.1 Compute the low-rank test image via multi-slice LRTD:

$$I_{LR_t}^k \leftarrow \text{MS-LRTD}(\mathcal{X}_t = [\hat{\mathcal{D}}_1^k, \hat{\mathcal{D}}_2^k, \dots, \hat{\mathcal{D}}_{N_c}^k, \mathcal{D}_t]).$$

3.2 Compute the non-rigid transformation T_i^k that warps \hat{I}_i to $I_{LR_t}^k$:

$$\hat{I}_i^{(k+1)} \leftarrow T_i^k(\hat{I}_i), i = 1, \dots, N_c, \text{ and obtain the corresponding third-order image tensors: } \hat{\mathcal{D}}_i^{(k+1)} \leftarrow \hat{I}_i^{(k+1)}, i = 1, \dots, N_c.$$

end for

$$I_{LR_t} \leftarrow I_{LR_t}^{N_{max}}.$$

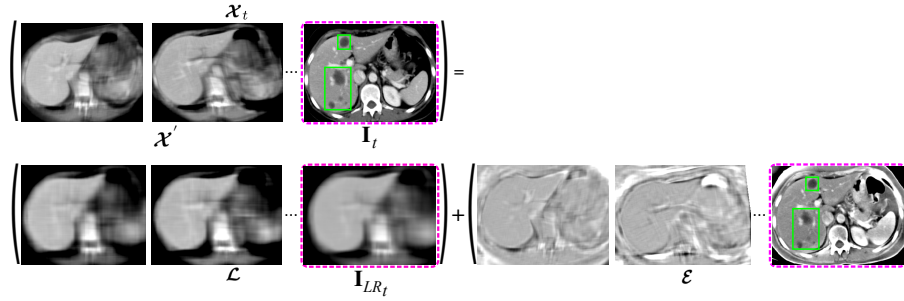


Figure 4: An example of generating the tumor-free image I_{LR_t} for a test liver image I_t (indicated by the pink dashed-line rectangle in \mathcal{X}_t) using the proposed low-rank tensor decomposition based probabilistic atlas (LRTD-PA). The data tensor \mathcal{X}_t is decomposed into a low-rank component \mathcal{L} corresponding to the tumor-free liver images, and a sparse component \mathcal{E} corresponding to the sparse tumors (indicated by green rectangles). For the purpose of illustration, it only shows one specific 2D slice of the CT volume.

Firstly, all intensity images of the tumor-free liver atlases within the chosen cluster c $\{\hat{I}_i \mid i = 1, \dots, N_c\}$ are non-rigidly warped to the space of I_{LR_t} , resulting in N_c non-rigid transformations $\{T_i \mid i = 1, \dots, N_c\}$. These non-rigid transfor-

Table 1: Specifications of the CT scans from the three databases.

| Database | Number of scans | In-plane matrix size | In-plane resolution [mm] | Number of slices | Slice thickness [mm] |
|----------------|-----------------|----------------------|--------------------------|------------------|----------------------|
| SLIVER07-Train | 20 | 512×512 | 0.58-0.81 | 64-394 | 0.7-5.0 |
| 3Dircadb1 | 20 | 512×512 | 0.56-0.86 | 74-260 | 1.0-4.0 |
| CT-ORG-Test | 21 | 512×512 | 0.65-1.37 | 75-841 | 0.8-5.0 |

mations then propagate the corresponding label images $\{L_i \mid i = 1, \dots, N_c\}$ into the space of I_{LR_t} , resulting in the propagated atlas labels $\{L'_i \mid i = 1, \dots, N_c\}$.

Finally, the N_c propagated atlas labels are combined via label fusion to obtain the liver segmentation result. Specifically, we adopt the joint label fusion (JLF) algorithm (Wang et al., 2013) considering its high performance. The JLF is a statistical local weighted label fusion algorithm, where the optimal weights for label fusion are obtained by minimizing the total expectation of labeling errors. Moreover, the pairwise correlation between atlases is explicitly modeled as the joint probability of two atlases creating a segmentation error at a voxel. Please refer to Wang et al. (2013) for more details on the JLF algorithm. To obtain the final segmentation result from the posterior probability map of liver likelihood produced by the JLF algorithm, it performs a series of simple post-processing operations on the probability map, consisting of thresholding using Otsu’s method (Otsu, 1979), morphological opening operator to remove small unconnected components and the noise, and morphological closing operator to fill small cavities.

5. Experiments

5.1. Datasets

In order to evaluate the performance of the proposed MAS framework, and to show its clinical applicability, we tested it on a clinical dataset of 61 abdominal CT scans of pathological liver cases from three publicly available databases. Table 1 outlines the specifications of the CT scans from the three databases.

Both SLIVER07-Train ¹ and 3Dircadb1 ² include 20 abdominal CT scans with corresponding ground truths, provided by the organizers of the Segmentation of the Liver Competition 2007 (SLIVER07) (Heimann et al., 2009), and IRCAD (Soler et al., 2009), the French Research Institute against Digestive Cancer, respectively. The CT-ORG-Test ³ consists of 21 abdominal CT scans with corresponding ground truths (Rister et al., 2020). Most of the cases in

¹<http://www.sliver07.org>

²<http://www.ircad.fr/software/3Dircadb/3Dircadb1/index.php?lng=en>

³<https://wiki.cancerimagingarchive.net/display/Public/CT-ORG%3A+CT+volumes+with+multiple+organ+segmentations>

the three databases were with hypodense and/or hyperdense tumor contrast levels, mainly including hepatocellular carcinoma (HCC), metastases, hemangiomas, and cysts of different size. The CT scans in the three databases were acquired by a wide variety of CT scanners from different vendors. In this study, the SLIVER07-Train database was employed to train the models, and to determine the parameter settings of the proposed method. The other two databases were only used to evaluate the segmentation performance, and to compare our method with state-of-the-art methods.

5.2. Evaluation Metrics and Statistical Hypothesis Testing

In order to perform quantitative evaluations of segmentation accuracy, the following two volume and surface based metrics are employed:

- (1) Jaccard index (*JI*) (Jaccard, 1901) measures the volumetric overlap between two segmentation results A and B , defined as:

$$JI(A, B) = \frac{|V(A) \cap V(B)|}{|V(A) \cup V(B)|} \times 100, \quad (12)$$

where $V(X)$ denotes the binary volume of segmentation result X .

- (2) Average symmetric surface distance (*ASD*) is the average distance between the surfaces of two segmentation results A and B (Heimann et al., 2009):

$$ASD(A, B) = \frac{\sum_{s_A \in S(A)} d(s_A, S(B)) + \sum_{s_B \in S(B)} d(s_B, S(A))}{|S(A)| + |S(B)|}, \quad (13)$$

where $d(v, S(X))$ is the shortest Euclidean distance from a voxel v to the surface voxels of segmentation result X .

The units of *JI* and *ASD* are percent and millimeters, respectively. For *JI* (*ASD*), the larger (smaller) the value is, the more accurate the segmentation result will be.

In order to determine whether the differences in segmentation accuracy between our method and other compared methods were statistically significant in the experiments, the paired t -test was carried out with a significance level of $p < 0.05$. The null hypothesis is that the mean values of the same evaluation metric are exactly the same for the compared methods.

5.3. Implementation Details

To reduce image noise without deteriorating the important edge information, it first preprocessed all training and test images via the 3D anisotropic diffusion filter (Perona and Malik, 1990). To perform the pairwise non-rigid image registrations, it utilized the publicly available elastix toolbox⁴ (Klein et al., 2010),

⁴<http://elastix.isi.uu.nl>

Table 2: Parameter settings for the proposed segmentation framework.

| Parameter | Value | Description |
|-----------|-------------|--|
| k | 3 | Number of training data clusters for LRTD-PA |
| K | 5 | Number of consecutive image slices for the multi-slice LRTD scheme |
| λ | λ_0 | Parameter in Eq. 10 for LRTD-PA. $\lambda_0 = 1/\sqrt{\max(n_1, n_2)n_3}$ is the default value for λ as suggested in Lu et al. (2020), where (n_1, n_2, n_3) is the size of the data tensor. |
| N_{max} | 3 | Maximum number of iterations in Algorithm 1 and Algorithm 2 |

in which the cubic B-spline based free-form deformation (FFD) model (Rueckert et al., 1999) with normalized mutual information (NMI) (Studholme et al., 1999) as the similarity measure was applied. The JLF algorithm implemented in the open source PICSL Multi-Atlas Segmentation Tool ⁵ (Wang and Yushkevich, 2013) was employed to perform label fusion. In Algorithm 1, the masked training images via liver binary masks were used to obtain all the non-rigid transformations, which were then propagated to the original training images. While only the original training and test images were used in Algorithm 2.

The parameter settings for the proposed MAS framework were optimized via leave-one-out cross-validation (LOOCV) using the SLIVER07-Train database. Table 2 lists the parameter settings for the proposed segmentation framework.

In the experiments, it compared the proposed LRTD-based MAS framework with two other closely related MAS frameworks: conventional MAS and the LRMD-based MAS. The latter one can be considered as a special case of the proposed framework, by substituting LRTD with LRMD to generate tumor-free liver images. Refer to Shi et al. (2017) for more details. To make the comparisons between different frameworks fair, the same training data clustering, non-rigid registration, and the JLF steps were utilized. Furthermore, we compared the proposed segmentation framework with other state-of-the-art methods.

All the MAS frameworks were implemented in Python on Ubuntu 18.04. The SimpleITK library (Yaniv et al., 2018) was utilized to perform the image processing. All the tests in this study were run on a PC equipped with an Intel Core i7 processor and 32 GB RAM. The average time to segment one test image was about 95 min, most of which was spent performing the pairwise non-rigid image registrations and the JLF, with an average time of about 3 min (per image registration) and 15 min, respectively.

⁵https://www.nitrc.org/projects/picsl_malf

Table 3: Quantitative comparative results of the masked tumor-free liver images with different choices of the transform matrix \mathbf{M} using the SLIVER07-Train database.

| Metrics | Initial | FFT | DWT | DCT |
|------------|------------|--------------|------------|-------------------|
| σ | 32.44±8.99 | 17.02±4.51 | 16.64±4.39 | 15.38±4.17 |
| H [bits] | 1.38±0.37 | 1.23±0.32 | 1.20±0.31 | 1.13±0.30 |
| Time [ms] | | 172.25±14.61 | 76.23±7.74 | 63.68±3.88 |

For each metric, the mean and standard deviation of the overall datasets are given.

Bold values are the best result in that column.

6. Results

6.1. Parameter Settings for the Liver Atlas Construction Method LRTD-PA

6.1.1. The Transform Matrix \mathbf{M}

An important implementation in the proposed liver atlas construction method LRTD-PA is to choose the best transform matrix \mathbf{M} of \star_M -product in Section 3.2, which converts the data tensor \mathcal{X} into other transform domain as $\tilde{\mathcal{X}}$. To this end, we tested the effect of three commonly used transforms (Kernfeld et al., 2015), i.e., FFT, DCT, and Daubechies-4 discrete wavelet transform (DWT), on the image intensity standard deviation σ and entropy H of the masked tumor-free liver images via liver binary masks. Since the smaller the σ and H are, the more homogeneous and smooth the appearance of the generated tumor-free liver image will be (Liu et al., 2015).

Table 3 shows the σ and H of the masked tumor-free liver images with different choices of the transform matrix \mathbf{M} using the SLIVER07-Train database. Although all the three transform matrices largely reduce the values of σ and H compared to their initial values of 32.44 and 1.38, respectively, the DCT achieves the smallest mean σ of 15.38, which is less than half of its initial value. Also, the DCT yields the smallest mean H of 1.13. The time needed to perform the multi-slice LRTD on each image segment is also given in Table 3. The DCT is the most efficient and only takes 63.68 ms, while FFT costs nearly three times of that for the same task. Therefore, we choose the DCT as the transform matrix \mathbf{M} for the proposed LRTD-PA.

6.1.2. The Number of Consecutive Image Slices for the Multi-Slice LRTD

The main aim of the proposed multi-slice LRTD scheme is to generate accurate tumor-free liver images, while coping with the rapid changes of both background and liver tissue over the whole image volume. An important hyper-parameter for the multi-slice LRTD scheme is the number of consecutive image slices K , which determines how many neighboring slices are used to perform the LRTD. To select the best K for this study, it tested the effect of different choices of K (from 2 to 11) on the image intensity standard deviation σ of the masked tumor-free liver images via liver binary masks.

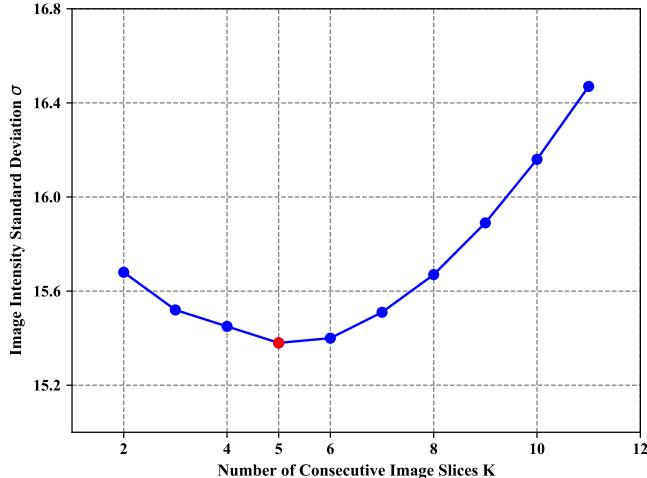


Figure 5: Image intensity standard deviation σ of the masked tumor-free liver images with different choices of the number of consecutive image slices K for the multi-slice LRTD scheme using the SLIVER07-Train database.

Fig. 5 shows the σ of the masked tumor-free liver images with different choices of K using the SLIVER07-Train database. It can be seen that the value of σ first decreases as the number of K increases. However, the value of σ begins to increase when $K > 5$, and the multi-slice LRTD scheme achieves the smallest value of σ when $K = 5$. Therefore, we choose $K = 5$ for the multi-slice LRTD scheme in this study. Note here that we only give the results of σ with regards to different K values, since the use of image intensity entropy H yields the same best choice $K = 5$.

6.2. Pathological Liver Segmentation of CT Images

In this section, to show the effectiveness of the proposed LRTD-based MAS framework, we applied it to the challenging task of pathological liver segmentation of CT images in the 3Dircadb1 database. It also compared the proposed method with two other closely related MAS frameworks, i.e., conventional MAS and the LRMD-based MAS, to verify its superiority. To make the comparisons between different MAS frameworks fair, the same training data clustering, non-rigid registration, and the JLF steps were utilized.

Fig. 6 shows the visually comparative results of the three population-specific liver PAs generated by the conventional PA, the LRMD-PA, and the proposed LRTD-PA. We can easily see that large areas of the PAs constructed by the conventional method appear totally different from that of the normal liver tissue (indicated by black arrows). Thus, the conventional method is strongly influenced by the presence of major pathology in training data. In comparison, the

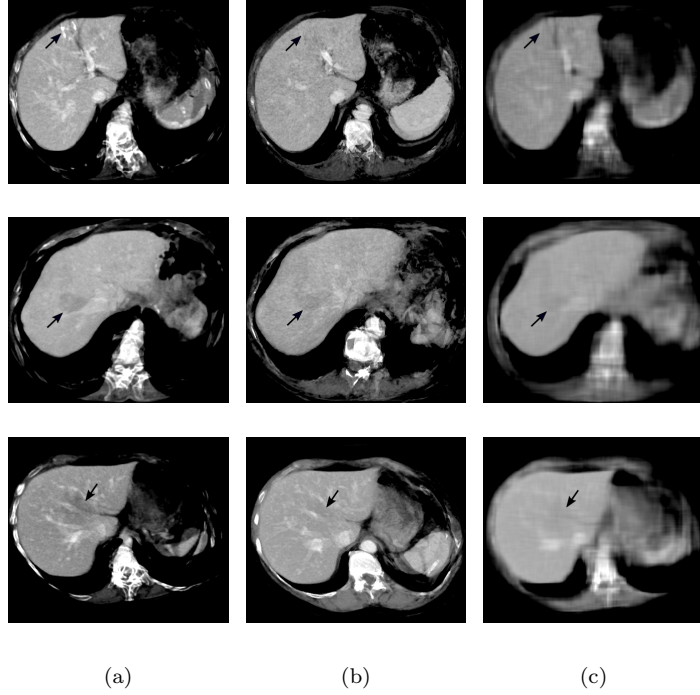


Figure 6: Comparative results of the three population-specific probabilistic atlases (PAs) generated by the conventional PA (1st column), the LRMD-PA (2nd column), and the proposed LRTD-PA (3rd column). Each row shows the PA of one training data cluster. The areas indicated by black arrows in the PAs of the conventional PA appear totally different from that of the normal liver tissue.

liver tissue of the PAs constructed by the LRMD-PA and our method appears more homogeneous, due to the use of tumor-free training images, which also leads to much more accurate pairwise image registrations. Nevertheless, compared with the LRMD-PA, our results are even more homogeneous and smooth, especially in areas containing major pathology and vessels. It is mainly because our tensor-based method can fully exploit the high correlations between neighboring slices of the 3D CT scans. While the LRMD-PA reformats the data tensor to a matrix by vectorizing voxel intensity values of each CT scan to form the column vectors, where the local spatial information is totally lost, and the multi-dimensional structure embedded in the tensor data is ignored, causing severe performance degradation. Therefore, our method can handle major pathology more effectively, and can mitigate the performance degradation of liver segmentation caused by the presence of tumors in the constructed atlases.

Fig. 7 gives the tumor-free liver images for three challenging pathological cases generated by the proposed LRTD-PA method, consisting of liver tissue with hypodense tumor, hyperdense tumor, and hypo- and hyperdense tumors

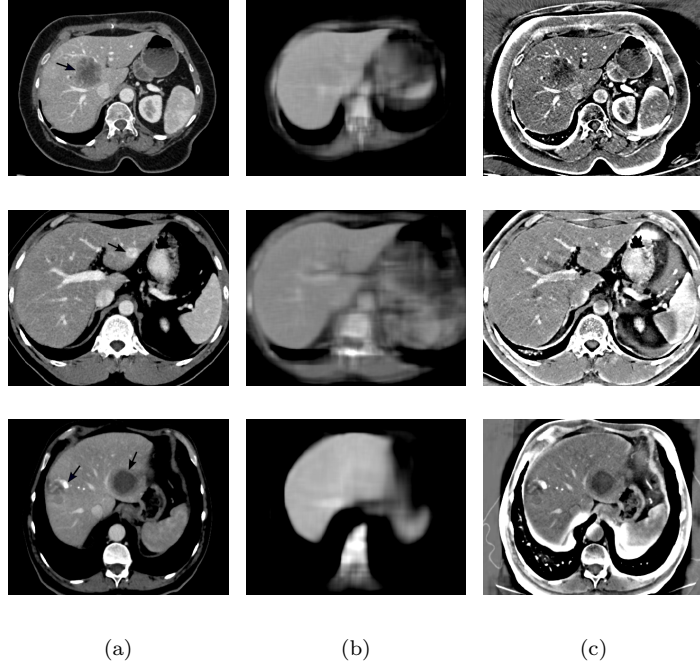


Figure 7: Results of the tumor-free liver images for three challenging pathological cases generated by the proposed LRTD-PA method, consisting of liver tissue with hypodense tumor (1st row), hyperdense tumor (2nd row), and hypo- and hyperdense tumors (3rd row) indicated by black arrows. In each row, (a) the original images, (b) the corresponding tumor-free images (low-rank components), and (c) sparse tumors (sparse components) are displayed sequentially.

(indicated by black arrows). For all the three challenging cases, our method successfully eliminates the tumors with different contrast levels from the original images as the sparse components. And the liver tissue in the decomposed low-rank components appears much more homogeneous and smooth than that in the original images. Thus, by eliminating the influence of major pathology, the proposed LRTD-based MAS algorithm can achieve accurate pairwise image registration and label propagation. Furthermore, it shows that the proposed multi-slice LRTD scheme is able to successfully recover the underlying low-rank structure embedded in 3D medical images.

Fig. 8 shows the visual results of liver segmentation generated by the conventional MAS, the LRMD-based MAS, and our proposed LRTD-based MAS frameworks on three challenging pathological cases, consisting of liver tissue with hypodense tumor, hyperdense tumor, and hypo- and hyperdense tumors (indicated by white arrows). Each row shows one case. The first case is a very challenging one, where the peripheral hypodense tumor (indicated by the upper left white arrow) has very similar intensity values to that of the nearby muscle tissue. We can see that the segmentation results of both the conventional

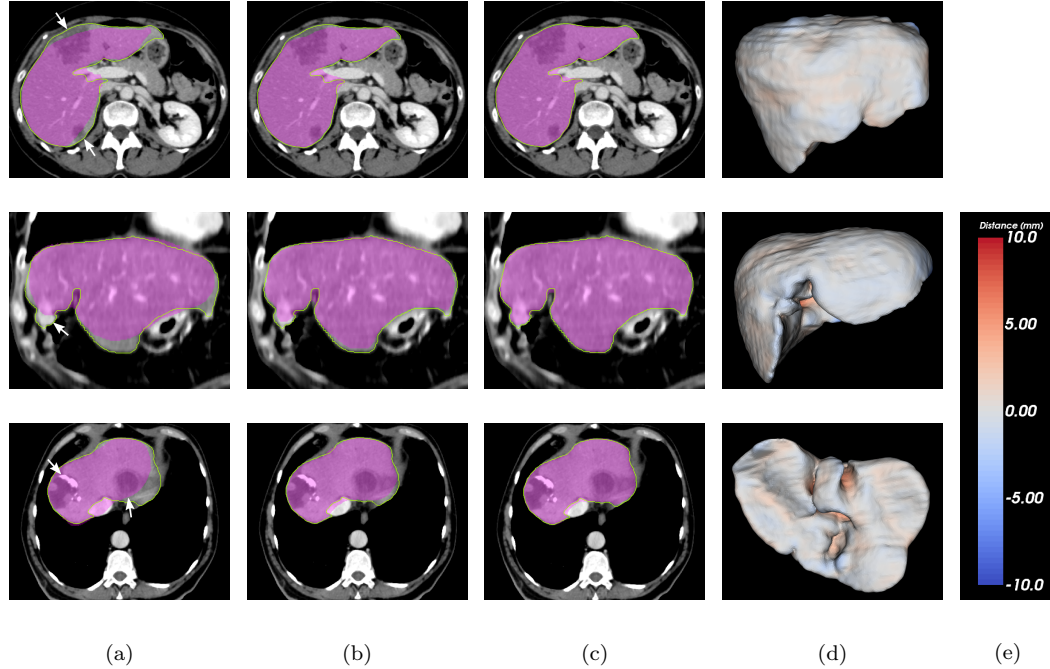


Figure 8: Results of liver segmentation by (a) the conventional MAS, (b) the LRMD-based MAS, and (c) the proposed LRTD-based MAS frameworks on three challenging pathological cases, consisting of liver tissue with hypodense tumor (1st row), hyperdense tumor (2nd row) and hypo- and hyperdense tumors (3rd row), indicated by white arrows. The ground truths are delineated by green contours, while the segmentation results are shown as pink regions. (d) The 3D visualization of average symmetric surface distance (ASD) errors of our method. The red and blue regions indicate over- and under-segmentation, respectively. (e) The distance to color bar.

MAS and the LRMD-based MAS exclude part of the peripheral pathological areas, thus resulting in under-segmentation. It is mainly due to the blurred boundaries between the peripheral hypodense tumor and the nearby muscle tissue, leading to inaccurate pairwise image registration and label propagation in the peripheral pathological areas. While our method accurately delineates the peripheral pathological areas, and yields more accurate segmentation results. This is mainly because by generating more accurate tumor-free liver images, our method can more effectively mitigate the performance degradation of liver segmentation due to the presence of tumors, compared to both the conventional MAS and the LRMD-based MAS.

In the second and the third cases, the liver tumors are also located near the boundary of the liver tissue. As expected, due to the inaccurate pairwise image registration in the peripheral pathological areas, the segmentation result of the conventional MAS excludes a large portion of the peripheral liver

Table 4: Comparative results of liver segmentation with three different MAS frameworks using the 3Dircadb1 database.

| Method | JI [%] | ASD [mm] |
|---------------------------|-------------------|------------------|
| Conventional MAS | 84.90±4.94* | 2.85±1.26* |
| LRMD-based MAS | 90.53±2.30* | 1.67±0.47* |
| Our LRTD-based MAS | 92.11±0.95 | 1.37±0.21 |

For each metric, the mean and standard deviation of the overall datasets are given. Bold values are the best result in that column. * indicates a statistically significant difference between the marked result and the corresponding one of our method at a significance level of 0.05.

tissue, and thus under-segmenting the live tissue. On the other hand, both the LRMD-based MAS and our method successfully delineate the boundaries near the peripheral pathological areas, and the segmentation results are much more accurate. This is because in both methods, the negative influence of these tumors on liver segmentation results can be largely mitigated by generating tumor-free liver images. However, our method recovers more finer edge details and yields more accurate result than the LRMD-based MAS, due to the use of more homogeneous and smooth tumor-free liver images, which lead to more accurate pairwise image registration and label propagation. These results demonstrate the strong robustness of our method to both hypodense and hyperdense tumor contrast levels.

Table 4 lists the quantitative comparative results of liver segmentation with three different MAS frameworks, i.e., the conventional MAS, the LRMD-based MAS, and the proposed LRTD-based MAS, using the 3Dircadb1 database. For each metric, the mean and standard deviation of the overall datasets are given. It can be observed that our LRTD-based MAS yields the best segmentation accuracy with the lowest variances in terms of both *JI* and *ASD*, demonstrating the robustness of our method on a variety of test data. Furthermore, our method outperforms the other two compared methods by a large margin, and statistically significant improvements ($p < 0.05$) over both the conventional MAS and the LRMD-based MAS were observed according to *JI* as well as *ASD*. In particular, the mean *JI* and mean *ASD* of our method are 92.11% and 1.37 mm, respectively. For the conventional MAS, the obtained mean *JI* (*ASD*) is quite low (high), with a value below 85% (above 2.80 mm). Compared to the LRMD-based MAS, our method achieves an average improvement of 1.58% and 18% according to *JI* and *ASD*, respectively. The above results therefore clearly indicate that our proposed method is significantly more accurate and robust than both the conventional MAS and the LRMD-based MAS in the presence of major pathology.

6.3. Comparison with State-of-the-art Methods

In this section, we compared our proposed MAS-based liver segmentation framework with state-of-the-art automatic methods using public databases to evaluate its performance relative to the wider context of existing works.

We first compare our proposed liver segmentation framework with state-of-the-art automatic methods using the 3Dircadb1 database. Table 5 outlines the quantitative results of liver segmentation of all the compared methods, including both deep learning based methods and model-based methods. As can be seen, among all the 11 compared methods, our method achieves the best performance, i.e., the largest (smallest) value of JI (ASD). Also, our method yields very small variances in terms of both JI and ASD , suggesting its robustness on a variety of datasets. Among deep learning based methods, the cascaded U-Net method proposed by Christ et al. (2017) obtains the best accuracy, with the mean JI and ASD of 89.30 % and 1.50 mm, respectively. However, the performance obtained by all other deep learning based methods is inferior to that of all the model-based methods (including MAS, ASM and graph cut) in terms of ASD . Although deep learning based methods are currently considered very good for medical image segmentation, their performance is strongly dependent on the availability of massive amounts of annotated training data. Moreover, the lack of interpretability remains a major constraint to the adoption of deep learning based methods in clinical applications, where interpretability of the obtained results is of paramount importance. Therefore, in clinical applications where the amount of annotated training data is low and a high level of trust is required (such as this study), model-based methods are still preferable to deep learning based methods.

Furthermore, we compared the proposed liver segmentation framework with state-of-the-art deep learning based method using the CT-ORG-Test database. The quantitative results of the compared methods are summarized in Table 6. We can see that as on the 3Dircadb1 database, our method is superior to the 3D U-Net (with data augmentation) method proposed by Rister et al. (2020) in terms of JI , with an average improvement of 0.76 %. It achieved a relatively small value of ASD compared to our method, but with a much larger variance, suggesting a low robustness. Also, their method required substantially more training data (119) than ours (20). Specifically, the mean JI and ASD of our method are 91.60 % and 1.44 mm, respectively. Furthermore, the performance obtained by Rister et al. (2020) degraded a lot when data augmentation was not applied, with the mean value of JI dropped from 90.84 % to 85.19 %, and the mean value of ASD increased from 1.09 mm to 1.21 mm.

All the above experimental results indicate that the performance of our method is more accurate and robust than that of state-of-the-art methods, including both deep learning based methods and model-based methods. Furthermore, the results demonstrate the strong robustness of our method against different tumor contrast levels. Therefore, the proposed MAS-based liver segmentation framework can be utilized for accurate and robust liver segmentation in the presence of major pathology.

Table 5: Comparison of the proposed method and state-of-the-art automatic methods using the 3Dircadb1 database.

| Method | Segmentation Framework | JI [%] | ASD [mm] |
|------------------------------------|------------------------|-------------------|------------------|
| <i>Deep learning based methods</i> | | | |
| Jiang et al. (2019) | AHCNet | 89.57 | N/A |
| Li et al. (2018) | H-DenseUNet | 89.98±3.44 | 4.06±3.85 |
| Kavur et al. (2020) | Ensembles of DMs | 85.19 | 3.07 |
| Lu et al. (2017) | CNN+GC | 90.64±3.34 | 1.89±1.08 |
| Christ et al. (2017) | Cascaded U-Net | 89.30 | 1.50 |
| <i>Model-based methods</i> | | | |
| Lu et al. (2018) | GC | 90.79±2.64 | 1.75±1.41 |
| Erdt and Kirschner (2010) | ASM | 89.66±3.11 | 1.74±0.59 |
| Esfandiarkhani and Foruzan (2017) | ASM | 89.61±2.45 | 1.66±0.48 |
| Li et al. (2015) | GC | 90.85±1.44 | 1.55±0.39 |
| Shi et al. (2016) | ASM | 91.26±2.37 | 1.45±0.37 |
| Our method | MAS | 92.11±0.95 | 1.37±0.21 |

Bold values are the best result in that column. ASM, GC and DM stand for active shape model, graph cut and deep learning model, respectively. N/A stands for Not Available information.

Table 6: Comparison of the proposed method and state-of-the-art deep learning based method using the CT-ORG-Test database.

| Method | Segmentation Framework | JI [%] | ASD [mm] |
|----------------------|------------------------|-------------------|------------------|
| Rister et al. (2020) | 3D U-Net (Without DA) | 85.19 | 1.21±1.55 |
| Rister et al. (2020) | 3D U-Net (With DA) | 90.84 | 1.09±1.19 |
| Our method | MAS | 91.60±1.04 | 1.44±0.17 |

Bold values are the best result in that column. DA stands for Data Augmentation.

7. Conclusion

In this paper, we propose a novel automatic method for accurate and robust pathological liver segmentation of CT images, by integrating the general \star_M -product based LRTD theory into the widely used MAS framework. Our method significantly enhances the traditional MAS framework in three directions, by proposing a multi-slice LRTD scheme, an LRTD-based atlas construction method, and an LRTD-based MAS algorithm.

To demonstrate the effectiveness of our proposed segmentation framework, we conducted extensive experiments using a total of 61 clinical CT scans of pathological liver cases from three publicly available databases, and our method yielded high performance. All the experimental results indicate that:

- The proposed multi-slice LRTD scheme is able to successfully recover the underlying low-rank structure embedded in 3D medical images.
- The proposed liver atlas construction method LRTD-PA yields much more homogeneous and smooth tumor-free liver atlases than both the conventional PA and the LRMD-PA methods.
- The proposed LRTD-based MAS algorithm derives very patient-specific liver atlases for each test image, and achieves accurate pairwise image registration and label propagation.
- The performance of our proposed segmentation framework is superior to that of state-of-the-art methods, including deep learning based methods and model-based methods.

In future studies, we plan to further improve its performance in two aspects: (1) In the proposed multi-slice LRTD scheme, both the \star_M -product and the tensor nuclear norm depend on the transformation matrix \mathbf{M} utilized. We may further increase the accuracy of tensor decomposition by learning the optimal transformation matrix (Lu and Zhou, 2019). (2) Currently, the computational cost of our method is still a little high. It is mainly due to the computationally intensive nature of the pairwise non-rigid image registrations. We will consider using deep learning-based registration methods, e.g., the VoxelMorph (Balakrishnan et al., 2019), to perform the image registrations to decrease the computational time of our segmentation framework.

Acknowledgment

This work was supported in part by the National Natural Science Foundation of China under Grant No. 61701178, and the Natural Science Foundation of Hunan Province of China (No. 2018JJ3256), and the China Scholarship Council (No. 201908430083).

Appendix A. Tensor Preliminaries

$$\text{bcirc}(\mathcal{X}) = \begin{bmatrix} \mathbf{X}^{(1)} & \mathbf{X}^{(n_3)} & \dots & \mathbf{X}^{(2)} \\ \mathbf{X}^{(2)} & \mathbf{X}^{(1)} & \dots & \mathbf{X}^{(3)} \\ \vdots & \vdots & \ddots & \vdots \\ \mathbf{X}^{(n_3)} & \mathbf{X}^{(n_3-1)} & \dots & \mathbf{X}^{(1)} \end{bmatrix}. \quad (\text{A.1})$$

$$\text{unfold}(\mathcal{X}) = \begin{bmatrix} \mathbf{X}^{(1)} \\ \mathbf{X}^{(2)} \\ \vdots \\ \mathbf{X}^{(n_3)} \end{bmatrix}, \quad \text{fold}(\text{unfold}(\mathcal{X})) = \mathcal{X}. \quad (\text{A.2})$$

$$\bar{\mathbf{X}} = \text{bdiag}(\bar{\mathcal{X}}) = \begin{bmatrix} \bar{\mathbf{X}}^{(1)} & & & \\ & \bar{\mathbf{X}}^{(2)} & & \\ & & \ddots & \\ & & & \bar{\mathbf{X}}^{(n_3)} \end{bmatrix}. \quad (\text{A.3})$$

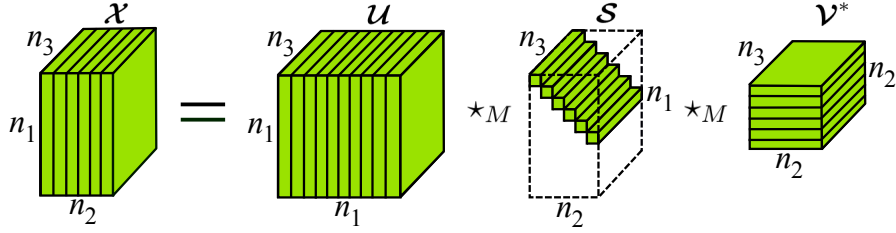


Figure A.9: An illustration of the t-SVD factorization of an $n_1 \times n_2 \times n_3$ tensor \mathcal{X} .

Algorithm 3 The T-SVD Algorithm under Transformation Matrix \mathbf{M}

Input: tensor $\mathcal{X} \in \mathbb{R}^{n_1 \times n_2 \times n_3}$ and invertible transformation matrix $\mathbf{M} \in \mathbb{R}^{n_3 \times n_3}$.

Output: $\mathbf{U} \in \mathbb{R}^{n_1 \times n_1 \times n_3}$, $\mathbf{S} \in \mathbb{R}^{n_1 \times n_2 \times n_3}$, $\mathbf{V} \in \mathbb{R}^{n_2 \times n_2 \times n_3}$.

1. Convert data into transform domain: $\bar{\mathcal{X}} \leftarrow \mathbf{M}(\mathcal{X})$.
 2. Compute matrix SVD for each frontal slice:
 $[\bar{\mathbf{U}}^{(k)}, \bar{\mathbf{S}}^{(k)}, \bar{\mathbf{V}}^{(k)}] \leftarrow \text{svd}(\bar{\mathcal{X}}^{(k)}), k = 1, \dots, n_3$.
 3. Convert data back to spatial domain:
 $\mathbf{U} \leftarrow \mathbf{M}^{-1}(\bar{\mathbf{U}})$, $\mathbf{S} \leftarrow \mathbf{M}^{-1}(\bar{\mathbf{S}})$, $\mathbf{V} \leftarrow \mathbf{M}^{-1}(\bar{\mathbf{V}})$
-

Definition 1 (Conjugate transpose Kilmer et al. (2019)). Let $\mathbf{M} \in \mathbb{R}^{n_3 \times n_3}$ be any invertible matrix. The conjugate transpose of a tensor $\mathcal{X} \in \mathbb{R}^{n_1 \times n_2 \times n_3}$ is the tensor $\mathcal{X}^* \in \mathbb{R}^{n_2 \times n_1 \times n_3}$ satisfying $(\mathbf{M}(\mathcal{X}^*))^{(i)} = (\mathbf{M}(\mathcal{X})^{(i)})^*$ for $i = 1, 2, \dots, n_3$.

Definition 2 (Identity tensor Kilmer et al. (2019)). Let $\mathbf{M} \in \mathbb{R}^{n_3 \times n_3}$ be any invertible matrix. The tensor $\mathcal{I} \in \mathbb{R}^{n \times n \times n_3}$ is an identity tensor if each frontal slice of $\bar{\mathcal{I}} = \mathbf{M}(\mathcal{I})$ is an $n \times n$ identity matrix \mathbf{I}_n .

Definition 3 (Orthogonal tensor Kilmer et al. (2019)). Let $\mathbf{M} \in \mathbb{R}^{n_3 \times n_3}$ be any invertible matrix. A tensor $\mathcal{Q} \in \mathbb{R}^{n \times n \times n_3}$ is orthogonal if it satisfies:

$$\mathcal{Q}^* \star_M \mathcal{Q} = \mathcal{Q} \star_M \mathcal{Q}^* = \mathcal{I}. \quad (\text{A.4})$$

Definition 4 (F-diagonal tensor Kilmer et al. (2019)). A tensor is f-diagonal if each of its frontal slice is diagonal.

Appendix B. The Closed-Form Solutions to the TPCP Problem of LRTD-PA in Eq. 10 via the ADMM Algorithm

The augmented Lagrangian function to be minimized for the TPCP problem in Eq. 10 is given as follows (from now on the subscript j is omitted to simplify notation):

$$L_\mu(\mathcal{L}, \mathcal{E}, \mathcal{Y}) = \|\mathcal{L}\|_* + \lambda \|\mathcal{E}\|_1 + \langle \mathcal{Y}, \mathcal{X} - \mathcal{L} - \mathcal{E} \rangle + \frac{\mu}{2} \|\mathcal{X} - \mathcal{L} - \mathcal{E}\|_F^2, \quad (\text{B.1})$$

where \mathcal{Y} and $\mu > 0$ denote the Lagrange multiplier and penalty parameter, respectively. To solve the problem in Eq. B.1, the ADMM algorithm first decomposes it into the following two minimization subproblems:

$$\begin{aligned} \mathcal{L}_{k+1} &= \arg \min_{\mathcal{L}} L_{\mu_k}(\mathcal{L}, \mathcal{E}_k, \mathcal{Y}_k), \\ \mathcal{E}_{k+1} &= \arg \min_{\mathcal{E}} L_{\mu_k}(\mathcal{L}_{k+1}, \mathcal{E}, \mathcal{Y}_k). \end{aligned} \quad (\text{B.2})$$

Then \mathcal{L} and \mathcal{E} are updated alternately by minimizing the augmented Lagrangian function with the other fixed. Finally, the Lagrange multiplier \mathcal{Y} is updated according to the following rule:

$$\mathcal{Y}_{k+1} = \mathcal{Y}_k + \mu_k(\mathcal{X} - \mathcal{L}_{k+1} - \mathcal{E}_{k+1}). \quad (\text{B.3})$$

Furthermore, both minimization subproblems in Eq. B.2 have closed-form solutions.

(i) \mathcal{L} minimization subproblem:

Theorem 2 (Lu et al. (2020)). *Given a tensor $\mathcal{W} \in \mathbb{R}^{n_1 \times n_2 \times n_3}$ and $\tau > 0$, the optimal solution to the following minimization problem is given by:*

$$\mathbf{D}_\tau(\mathcal{W}) = \arg \min_{\mathcal{X}} \tau \|\mathcal{X}\|_* + \frac{1}{2} \|\mathcal{X} - \mathcal{W}\|_F^2, \quad (\text{B.4})$$

where \mathbf{D}_τ is the tensor singular value thresholding (t-SVT) operator (Lu et al., 2020) defined as: $\mathbf{D}_\tau(\mathcal{W}) = \mathbf{U} \star_M \mathbf{S}_\tau \star_M \mathbf{V}^*$, where $\mathbf{U} \star_M \mathbf{S}_\tau \star_M \mathbf{V}^* = \mathcal{W}$ is the t-SVD of \mathcal{W} , $\mathbf{S}_\tau = \mathbf{M}^{-1}(\mathbf{S}_\tau(\bar{\mathcal{S}}))$, and $\mathbf{S}_\tau(\bar{s}_{ijk}) = \max(|\bar{s}_{ijk}| - \tau, 0) \cdot \text{sgn}(\bar{s}_{ijk})$ is the shrinkage operator applied on $\bar{\mathcal{S}}$ element-wisely, where $\text{sgn}(\cdot)$ is the sign function.

Given the other variable fixed, the closed-form solution for \mathcal{L} subproblem in Eq. B.2 can be obtained as follows according to Theorem 2:

$$\begin{aligned}
\mathcal{L}_{k+1} &= \arg \min_{\mathcal{L}} L_{\mu_k}(\mathcal{L}, \mathcal{E}_k, \mathbf{Y}_k) \\
&= \arg \min_{\mathcal{L}} \|\mathcal{L}\|_* + \frac{\mu_k}{2} \|\mathcal{X} - \mathcal{L} - \mathcal{E}_k + \frac{\mathbf{Y}_k}{\mu_k}\|_F^2 \\
&= \mathbf{D}_{\frac{\mu_k}{2}}(\mathcal{X} - \mathcal{E}_k + \frac{\mathbf{Y}_k}{\mu_k}).
\end{aligned} \tag{B.5}$$

(ii) \mathcal{E} minimization subproblem:

Theorem 3 (Hale et al. (2008)). *Given a tensor $\mathcal{W} \in \mathbb{R}^{n_1 \times n_2 \times n_3}$ and $\tau > 0$,*

Algorithm 4 The ADMM Algorithm for Solving the TPCP Problem in Eq. 10

Input: Data tensor \mathcal{X} , weighting parameter λ .

Output: $\mathcal{L} = \mathcal{L}_{k+1}$, $\mathcal{E} = \mathcal{E}_{k+1}$.

1. Initialization:

$$\mathcal{L}_0 = \mathcal{E}_0 = \mathbf{Y}_0 = 0, \mu_0 = 10^{-3}, \mu_{max} = 10^{10}, \rho = 1.1, \varepsilon = 10^{-8}, \text{ and } k = 0.$$

2. Solving the TPCP problem iteratively:

while *Not Converged* **do**

2.1 Update \mathcal{L} :

$$\mathcal{L}_{k+1} \leftarrow \mathbf{D}_{\frac{\mu_k}{2}}(\mathcal{X} - \mathcal{E}_k + \frac{\mathbf{Y}_k}{\mu_k}).$$

2.2 Update \mathcal{E} :

$$\mathcal{E}_{k+1} \leftarrow \mathbf{S}_{\frac{\lambda}{\mu_k}}(\mathcal{X} - \mathcal{L}_{k+1} + \frac{\mathbf{Y}_k}{\mu_k}).$$

2.3 Check the convergence conditions:

if $\|\mathcal{L}_{k+1} - \mathcal{L}_k\|_\infty < \varepsilon$ **and** $\|\mathcal{E}_{k+1} - \mathcal{E}_k\|_\infty < \varepsilon$ **and** $\|\mathcal{X} - \mathcal{L}_{k+1} - \mathcal{E}_{k+1}\|_\infty < \varepsilon$ **then**

break.

end if

2.4 Update \mathbf{Y} :

$$\mathbf{Y}_{k+1} \leftarrow \mathbf{Y}_k + \mu_k(\mathcal{X} - \mathcal{L}_{k+1} - \mathcal{E}_{k+1}).$$

2.5 Update μ :

$$\mu_{k+1} \leftarrow \min(\rho\mu_k, \mu_{max}).$$

2.6 $k \leftarrow k + 1$.

end while

Algorithm 5 Optimization Procedure of the Multi-Slice LRTD Scheme

Input: Aligned training image tensors of cluster c : $\{\mathcal{D}_i \mid i = 1, \dots, N_c\}$, weighting parameter λ , and the segment length K .

Output: $\hat{\mathcal{L}}, \hat{\mathcal{E}}$.

1. Partition \mathcal{D}_i into N_s image segments consisting of multiple consecutive image slices of length K : $[\mathcal{D}_{i1}, \mathcal{D}_{i2}, \dots, \mathcal{D}_{iN_s}] \leftarrow \mathcal{D}_i, i = 1, \dots, N_c$.

2. Perform the LRTD on each image segment tensor:

for $j = 1$ **to** N_s **do**

2.1 $\mathcal{X}_j \leftarrow$ Construct an image repository tensor for segment j by using the corresponding training segments $\{\mathcal{D}_{ij} \mid i = 1, \dots, N_c\}$.

2.2 Use the ADMM Algorithm (Algorithm 4) to perform LRTD:

$$(\hat{\mathcal{L}}_j, \hat{\mathcal{E}}_j) \leftarrow \text{ADMM}(\mathcal{X}_j, \lambda).$$

end for

3. $(\hat{\mathcal{L}}, \hat{\mathcal{E}}) \leftarrow$ Stack $\{\hat{\mathcal{L}}_j \mid j = 1, \dots, N_s\}$, $\{\hat{\mathcal{E}}_j \mid j = 1, \dots, N_s\}$ frontal-slice-wisely.

the optimal solution to the following minimization problem is given by:

$$\mathbf{S}_\tau(\mathcal{W}) = \arg \min_{\mathcal{X}} \tau \|\mathcal{X}\|_1 + \frac{1}{2} \|\mathcal{X} - \mathcal{W}\|_F^2, \quad (\text{B.6})$$

where \mathbf{S}_τ is the shrinkage operator.

Similarly, the closed-form solution for \mathcal{E} subproblem in Eq. B.2 can be written as follows according to Theorem 3:

$$\begin{aligned} \mathcal{E}_{k+1} &= \arg \min_{\mathcal{E}} L_{\mu_k}(\mathcal{L}_{k+1}, \mathcal{E}, \mathcal{Y}_k) \\ &= \arg \min_{\mathcal{E}} \lambda \|\mathcal{E}\|_1 + \frac{\mu_k}{2} \|\mathcal{X} - \mathcal{L}_{k+1} - \mathcal{E} + \frac{\mathcal{Y}_k}{\mu_k}\|_F^2 \\ &= \mathbf{S}_{\frac{\lambda}{\mu_k}}(\mathcal{X} - \mathcal{L}_{k+1} + \frac{\mathcal{Y}_k}{\mu_k}). \end{aligned} \quad (\text{B.7})$$

References

- Ahn, S.H., Yeo, A.U., Kim, K.H., Kim, C., Goh, Y., Cho, S., Lee, S.B., Lim, Y.K., Kim, H., Shin, D., Kim, T., Kim, T.H., Youn, S.H., Oh, E.S., Jeong, J.H., 2019. Comparative clinical evaluation of atlas and deep-learning-based auto-segmentation of organ structures in liver cancer. *Radiation Oncology* 14, 1–13.
- Balakrishnan, G., Zhao, A., Sabuncu, M.R., Guttag, J.V., Dalca, A.V., 2019. VoxelMorph: A learning framework for deformable medical image registration. *IEEE Trans. Med. Imag.* 38, 1788–1800.

- Boyd, S., Parikh, N., Chu, E., Peleato, B., Eckstein, J., 2010. Distributed optimization and statistical learning via the alternating direction method of multipliers. *Foundations and Trends in Machine Learning* 3, 1–122.
- Bray, F., Ferlay, J., Soerjomataram, I., Siegel, R.L., Torre, L.A., Jemal, A., 2018. Global cancer statistics 2018: GLOBOCAN estimates of incidence and mortality worldwide for 36 cancers in 185 countries. *CA: A Cancer Journal for Clinicians* 68, 394–424.
- Christ, P.F., Ettlinger, F., Grün, F., Elshaer, M.E.A., Lipková, J., Schlecht, S., Ahmaddy, F., Tatavarty, S., Bickel, M., Bilic, P., Rempfler, M., Hofmann, F., D’Anastasi, M., Ahmadi, S., Kaissis, G., Holch, J., Sommer, W.H., Braren, R., Heinemann, V., Menze, B.H., 2017. Automatic liver and tumor segmentation of CT and MRI volumes using cascaded fully convolutional neural networks. *CoRR abs/1702.05970v2*, 1–20. URL: <https://arxiv.org/abs/1702.05970v2>.
- Cichocki, A., Mandic, D.P., Lathauwer, L.D., Zhou, G., Zhao, Q., Caiafa, C.F., Phan, A.H., 2015. Tensor decompositions for signal processing applications: From two-way to multiway component analysis. *IEEE Signal Process. Mag.* 32, 145–163.
- Dakua, S.P., Abi-Nahed, J., Al-Ansari, A., 2016. Pathological liver segmentation using stochastic resonance and cellular automata. *Journal of Visual Communication and Image Representation* 34, 89–102.
- Erdt, M., Kirschner, M., 2010. Fast automatic liver segmentation combining learned shape priors with observed shape deviation, in: *Proc. IEEE 23rd International Symposium on Computer-Based Medical Systems (CBMS 2010)*, Perth, Australia. pp. 249–254.
- Erdt, M., Steger, S., Sakas, G., 2012. Regmentation: A new view of image segmentation and registration. *Journal of Radiation Oncology Informatics* 4, 1–23.
- Esfandiarkhani, M., Foruzan, A.H., 2017. A generalized active shape model for segmentation of liver in low-contrast CT volumes. *Computers in Biology and Medicine* 82, 59–70.
- Fu, Y., Dong, W., 2016. 3D magnetic resonance image denoising using low-rank tensor approximation. *Neurocomputing* 195, 30–39.
- Hale, E.T., Yin, W., Zhang, Y., 2008. Fixed-point continuation for ℓ_1 -minimization: Methodology and convergence. *SIAM Journal on Optimization* 19, 1107–1130.
- Heimann, T., van Ginneken, B., Styner, M., Arzhaeva, Y., Aurich, V., Bauer, C., Beck, A., Becker, C., Beichel, R., Bekes, G., Bello, F., Binnig, G.K., Bischof, H., Bornik, A., Cashman, P., Chi, Y., Cordova, A., Dawant, B.M., Fidrich,

- M., Furst, J.D., Furukawa, D., Grenacher, L., Hornegger, J., Kainmüller, D., Kitney, R., Kobatake, H., Lamecker, H., Lange, T., Lee, J., Lennon, B., Li, R., Li, S., Meinzer, H.P., Németh, G., Raicu, D.S., Rau, A., van Rikxoort, E.M., Rousson, M., Ruskó, L., Saddi, K.A., Schmidt, G., Seghers, D., Shimizu, A., Slagmolen, P., Sorantin, E., Soza, G., Susomboon, R., Waite, J.M., Wimmer, A., Wolf, I., 2009. Comparison and evaluation of methods for liver segmentation from CT datasets. *IEEE Trans. Med. Imag.* 28, 1251–1265.
- Heimann, T., Meinzer, H.P., 2009. Statistical shape models for 3D medical image segmentation: A review. *Medical Image Analysis* 13, 543–563.
- Hillar, C.J., Lim, L., 2013. Most tensor problems are NP-hard. *Journal of the ACM* 60, 45:1–45:39.
- Iglesias, J.E., Sabuncu, M.R., 2015. Multi-atlas segmentation of biomedical images: A survey. *Medical Image Analysis* 24, 205–219.
- Jaccard, P., 1901. Étude comparative de la distribution florale dans une portion des alpes et des jura. *Bulletin de la Société Vaudoise des Sciences Naturelles* 37, 547–579.
- Jiang, H., Shi, T., Bai, Z., Huang, L., 2019. AHCNet: An application of attention mechanism and hybrid connection for liver tumor segmentation in CT volumes. *IEEE Access* 7, 24898–24909.
- Jiang, X., Zhang, L., Qiao, L., Shen, D., 2020. Estimating functional connectivity networks via low-rank tensor approximation with applications to MCI identification. *IEEE Trans. Biomed. Eng.* 67, 1912–1920.
- Kavur, A.E., Kuncheva, L.I., Selver, M.A., 2020. Basic ensembles of vanilla-style deep learning models improve liver segmentation from CT images. *CoRR* abs/2001.09647, 1–10. URL: <https://arxiv.org/abs/2001.09647>.
- Kernfeld, E., Kilmer, M., Aeron, S., 2015. Tensor-tensor products with invertible linear transforms. *Linear Algebra and its Applications* 485, 545–570.
- Khaleel, H.S., Sagheer, S.V.M., Baburaj, M., George, S.N., 2018. Denoising of rician corrupted 3D magnetic resonance images using *tensor*-SVD. *Biomedical Signal Processing and Control* 44, 82–95.
- Kilmer, M., Horesh, L., Avron, H., Newman, E., 2019. Tensor-tensor products for optimal representation and compression. *CoRR* abs/2001.00046, 1–27. URL: <https://arxiv.org/abs/2001.00046>.
- Kilmer, M.E., Martin, C.D., 2011. Factorization strategies for third-order tensors. *Linear Algebra and its Applications* 435, 641–658.
- Klein, S., Staring, M., Murphy, K., Viergever, M.A., Pluim, J.P.W., 2010. elastix: A toolbox for intensity-based medical image registration. *IEEE Trans. Med. Imag.* 29, 196–205.

- Kobashi, M., Shapiro, L.G., 1995. Knowledge-based organ identification from CT images. *Pattern Recognition* 28, 475–491.
- Kolda, T.G., Bader, B.W., 2011. Tensor decompositions and applications. *SIAM review* 51, 455–500.
- Lee, P., Chan, C., Huang, S., Chen, A., Chen, H.H., 2018. Extracting blood vessels from full-field OCT data of human skin by short-time RPCA. *IEEE Trans. Med. Imag.* 37, 1899–1909.
- Li, G., Chen, X., Shi, F., Zhu, W., Tian, J., Xiang, D., 2015. Automatic liver segmentation based on shape constraints and deformable graph cut in CT images. *IEEE Trans. Image Process.* 24, 5315–5329.
- Li, X., Chen, H., Qi, X., Dou, Q., Fu, C., Heng, P., 2018. H-DenseUNet: Hybrid densely connected UNet for liver and tumor segmentation from CT volumes. *IEEE Trans. Med. Imag.* 37, 2663–2674.
- Li, Y., Zhao, Y., Zhang, F., Liao, M., Yu, L., Chen, B., Wang, Y., 2020. Liver segmentation from abdominal CT volumes based on level set and sparse shape composition. *Computer Methods and Programs in Biomedicine* 195, 105533.
- Litjens, G., Kooi, T., Bejnordi, B.E., Setio, A.A.A., Ciompi, F., Ghafoorian, M., van der Laak, J.A.W.M., van Ginneken, B., Sánchez, C.I., 2017. A survey on deep learning in medical image analysis. *Medical Image Analysis* 42, 60–88.
- Liu, X., Niethammer, M., Kwitt, R., Singh, N., McCormick, M., Aylward, S., 2015. Low-Rank Atlas Image Analyses in the Presence of Pathologies. *IEEE Trans. Med. Imag.* 34, 2583–2591.
- Liu, Y., Liu, T., Liu, J., Zhu, C., 2020. Smooth robust tensor principal component analysis for compressed sensing of dynamic MRI. *Pattern Recognition* 102, 107252.
- Lu, C., Feng, J., Chen, Y., Liu, W., Lin, Z., Yan, S., 2020. Tensor robust principal component analysis with a new tensor nuclear norm. *IEEE Trans. on Pattern Analysis and Machine Intelligence* 42, 925–938.
- Lu, C., Peng, X., Wei, Y., 2019. Low-rank tensor completion with a new tensor nuclear norm induced by invertible linear transforms, in: *Proc. IEEE Conference on Computer Vision and Pattern Recognition (CVPR’2019)*, Long Beach, California, USA. pp. 5996–6004.
- Lu, C., Zhou, P., 2019. Exact recovery of tensor robust principal component analysis under linear transforms. *CoRR* abs/1907.08288, 1–10. URL: <https://arxiv.org/abs/1907.08288>.
- Lu, F., Wu, F., Hu, P., Peng, Z., Kong, D., 2017. Automatic 3D liver location and segmentation via convolutional neural network and graph cut. *International Journal of Computer Assisted Radiology and Surgery* 12, 171–182.

- Lu, X., Xie, Q., Zha, Y., Wang, D., 2018. Fully automatic liver segmentation combining multi-dimensional graph cut with shape information in 3D CT images. *Scientific Reports* 8, 1–9.
- von Luxburg, U., 2007. A tutorial on spectral clustering. *Statistics and Computing* 17, 395–416.
- Madathil, B., Sagheer, S.V.M., V, A.R., Tom, A.J., S, B.P., Francis, J., George, S.N., 2019. Tensor low rank modeling and its applications in signal processing. *CoRR* abs/1912.03435, 1–24. URL: <https://arxiv.org/abs/1912.03435>.
- Natarajan, B.K., 1995. Sparse approximate solutions to linear systems. *SIAM Journal on Computing* 24, 227–234.
- Otsu, N., 1979. A threshold selection method from gray-level histograms. *IEEE Trans. Syst., Man, Cybern.* 9, 62–66.
- Perona, P., Malik, J., 1990. Scale-Space and Edge Detection Using Anisotropic Diffusion . *IEEE Trans. Pattern Anal. Mach. Intell.* 12, 629–639.
- Qin, B., Jin, M., Hao, D., Lv, Y., Liu, Q., Zhu, Y., Ding, S., Zhao, J., Fei, B., 2019. Accurate vessel extraction via tensor completion of background layer in x-ray coronary angiograms. *Pattern Recognition* 87, 38–54.
- Raju, A., Ji, Z., Cheng, C., Cai, J., Huang, J., Xiao, J., Lu, L., Liao, C., Harrison, A.P., 2020. User-guided domain adaptation for rapid annotation from user interactions: A study on pathological liver segmentation, in: *Proc. Medical Image Computing and Computer-Assisted Intervention (MICCAI’20)*, Lima, Peru. pp. 457–467.
- Rister, B., Yi, D., Shivakumar, K., Nobashi, T., Rubin, D.L., 2020. CT-ORG, a new dataset for multiple organ segmentation in computed tomography. *Scientific Data* 7, 1–9.
- Roohi, S.F., Zonoobi, D., Kassim, A.A., Jaremko, J.L., 2017. Multi-dimensional low rank plus sparse decomposition for reconstruction of under-sampled dynamic MRI. *Pattern Recognition* 63, 667–679.
- Rueckert, D., Sonoda, L.I., Hayes, C., Hill, D.L.G., Leach, M.O., Hawkes, D.J., 1999. Non-rigid registration using free-form deformations: Application to breast MR images. *IEEE Trans. Med. Imag.* 18, 712–721.
- Ruskó, L., Bekes, G., Fidrich, M., 2009. Automatic segmentation of the liver from multi- and single-phase contrast-enhanced CT images. *Medical Image Analysis* 13, 871–882.
- Sagheer, S.V.M., George, S.N., 2019. Denoising of low-dose CT images via low-rank tensor modeling and total variation regularization. *Artificial Intelligence in Medicine* 94, 1–17.

- Shi, C., Cheng, Y., Liu, F., Wang, Y., Bai, J., Tamura, S., 2016. A hierarchical local region-based sparse shape composition for liver segmentation in CT scans. *Pattern Recognition* 50, 88–106.
- Shi, C., Cheng, Y., Wang, J., Wang, Y., Mori, K., Tamura, S., 2017. Low-rank and sparse decomposition based shape model and probabilistic atlas for automatic pathological organ segmentation. *Medical Image Analysis* 38, 30–49.
- Shi, F., Cheng, J., Wang, L., Yap, P.T., Shen, D., 2015. LRTV: MR image super-resolution with low-rank and total variation regularizations. *IEEE Trans. Med. Imag.* 34, 2459–2466.
- Sidiropoulos, N.D., Lathauwer, L.D., Fu, X., Huang, K., Papalexakis, E.E., Faloutsos, C., 2017. Tensor decomposition for signal processing and machine learning. *IEEE Trans. Signal Process.* 65, 3551–3582.
- Sobral, A., Zahzah, E., 2017. Matrix and tensor completion algorithms for background model initialization: A comparative evaluation. *Pattern Recognition Letters* 96, 22–33.
- Soler, L., Hostettler, A., Agnus, V., Charnoz, A., Fasquel, J.B., Moreau, J., Osswald, A.B., Bouhadjar, M., Marescaux, J., 2009. 3D image reconstruction for comparison of algorithm database: A patient-specific anatomical and medical image database, in: *Proc. Workshop on Anatomical Models, Rocquencourt, France*. pp. 1–1. URL: <http://www-sop.inria.fr/geometrica/events/wam/abstract-ircad.pdf>.
- Studholme, C., Hill, D.L.G., Hawkes, D.J., 1999. An overlap invariant entropy measure of 3D medical image alignment. *Pattern Recognition* 32, 71–86.
- Umetsu, S., Shimizu, A., Watanabe, H., Kobatake, H., Nawano, S., 2014. An automated segmentation algorithm for CT volumes of livers with atypical shapes and large pathological lesions. *IEICE Transactions on Information and Systems* E97-D, 951–963.
- Wang, H., Suh, J.W., Das, S.R., Pluta, J., Craige, C., Yushkevich, P.A., 2013. Multi-atlas segmentation with joint label fusion. *IEEE Trans. on Pattern Analysis and Machine Intelligence* 35, 611–623.
- Wang, H., Yushkevich, P.A., 2013. Multi-atlas segmentation with joint label fusion and corrective learning - an open source implementation. *Frontiers Neuroinformatics* 7, 1–12.
- Xian, M., Zhang, Y., Cheng, H., Xu, F., Zhang, B., Ding, J., 2018. Automatic breast ultrasound image segmentation: A survey. *Pattern Recognition* 79, 340–355.

- Xu, Y., Duan, L., Fu, H., Zhang, X., Wong, D.W.K., Baskaran, M., Aung, T., Liu, J., 2016. Axial alignment for anterior segment swept source optical coherence tomography via robust low-rank tensor recovery, in: Proc. Medical Image Computing and Computer-Assisted Intervention (MICCAI'16), Athens, Greece. pp. 441–449.
- Yaniv, Z., Lowekamp, B.C., Johnson, H.J., Beare, R., 2018. SimpleITK image-analysis notebooks: a collaborative environment for education and reproducible research. *Journal of Digital Imaging* 31, 290–303.
- Zhang, F., Hou, J., Wang, J., Wang, W., 2020a. Uniqueness guarantee of solutions of tensor tubal-rank minimization problem. *IEEE Signal Process. Lett.* 27, 540–544.
- Zhang, F., Wang, J., Wang, W., Xu, C., 2020b. Low-tubal-rank plus sparse tensor recovery with prior subspace information. *IEEE Trans. Pattern Anal. Mach. Intell.* doi:<http://dx.doi.org/10.1109/TPAMI.2020.2986773>.
- Zhou, X., Yang, C., Zhao, H., Yu, W., 2014. Low-rank modeling and its applications in image analysis. *ACM Computing Surveys* 47, 36:1–36:33.